

WDL-TR2366
2 January 1965

POWER

COMET AND CLOSE-APPROACH ASTEROID MISSION STUDY

FINAL REPORT

VOL. 7

This work was performed for the Jet Propulsion Laboratory,
California Institute of Technology, sponsored by the
National Aeronautics and Space Administration under
Contract NAS7-100.

Prepared for
Jet Propulsion Laboratory
Pasadena, California

WDL-TR2366
2 January 1965

POWER

COMET AND CLOSE-APPROACH ASTEROID MISSION STUDY

FINAL REPORT

VOLUME 7

Contract JPL 950870

Prepared by

PHILCO CORPORATION
A Subsidiary of Ford Motor Company
WDL Division
Palo Alto, California

Prepared for

Jet Propulsion Laboratory
Pasadena, California

FOREWORD

This document is the final report of work performed on Power by the WDL Division of the Philco Corporation during the Comet and Close-Approach Asteroid Mission Study for the Jet Propulsion Laboratory under Contract JPL 950870. The report covers work performed during the period 2 July 1964 to 2 January 1965.

ACKNOWLEDGEMENT

The work on photovoltaic power was performed by John Fairbanks; the work on isotopic power and solar flare effects was performed by Wayne Picciano.

SUMMARY

PHOTOVOLTAIC

Components for the photovoltaic power subsystem have been selected on the basis of the current state-of-the-art utilizing test evaluation and flight data. Hence, the power output figures represent readily obtainable performance, which can be upgraded by incorporating future solar-cell panel developments. Experience gained on the MACS program, which aims at 1967-1970 flights, has been utilized. Four rectangular or trapezoidal panels with N/P silicon solar cells having 10 percent conversion efficiency installed over 85 percent of the frontal panel area have been considered for missions to six comets of interest. The design is based on a minimum-power output from the conditioning equipment of 200 watts at 28 volts after the panels have experienced a giant solar flare. The design points are the sun-probe distances at intercept. Batteries supply power during prelaunch, launch, solar panel deployment, peak loads, acquisition and maneuver.

ISOTOPIC POWER

The design and integration of a radioactive thermoelectric generator into an instrumented scientific probe vehicle is accomplished in three parts:

1. Design of the RTG unit
2. Determination of radiation sensitivity of instrumentation
3. Design and compatible placement of required instrument shielding.

For the purposes of this contract, a conceptual design of the RTG unit has been made and applied to provide the required weight-power comparisons. For plutonium systems, weight versus thermal power has been calculated for isotope, cladding, TE units, casing, fins, and miscellaneous construction materials. A projection of RTG power-to-weight ratios has been made using best available information from Martin, Battelle, Philco, and the literature.

A study to advance the state-of-the-art in shielding techniques forms the bulk of effort. A mathematical analysis employing the calculus of variations has produced a technique to determine the minimum-weight shape and location for a radiation shadow shield. A weight comparison between conventional and optimal shield configurations has been made. The determination of instrument sensitivity to radiation has not been made. It was hoped to include experimental data on this subject from an external source; the promised data has not yet reached Philco.

TABLE OF CONTENTS

<u>Section</u>		<u>Page</u>
1	OBJECTIVES AND REQUIREMENTS	1-1
	1.1 Background	1-1
	1.2 Requirements	1-1
2	PHOTOVOLTAIC POWER SUBSYSTEM	2-1
	2.1 Functional Description	2-1
	2.2 Photovoltaic Panel Design	2-6
	2.3 Batteries	2-13
3	GIANT SOLAR-FLARE EFFECTS	3-1
	3.1 Damage to Solar Cells	3-1
	3.2 Damage to Electronics	3-4
4	ISOTOPIC POWER SUBSYSTEM	4-1
	4.1 Thermoelectric Technology	4-1
	4.2 Fuel Availability	4-2
	4.3 Cold-Junction Temperature	4-2
	4.4 RTG Design	4-5
5	OPTIMUM SHIELDING CONFIGURATIONS	5-1
	5.1 Introduction	5-1
	5.2 Results of Study	5-1
	5.3 Analytical Development	5-9
6	CONCLUSIONS AND RECOMMENDATIONS	6-1
	6.1 Photovoltaic-Isotopic Comparison	6-1
	6.2 Choice of Power Subsystem	6-4
7	REFERENCES	7-1

APPENDIX

A	Calculation of Solar Cell Degradation Due to Protons	A-1
	A.1 Determination of Summation	A-1
	A.2 Derivation	A-3
B	Martin Company RTG Design (Confidential)	B-1

LIST OF ILLUSTRATIONS

<u>Figure</u>		<u>Page</u>
2-1	Solar Cell Current-Voltage Characteristics	2-2
2-2	Solar Panel Temperature and Power Corrected for Non-Ideal Thermal Conduction	2-10
2-3	Total Panel Area vs. Heliocentric Distance, Power and Cover-Glass Thickness	2-14
2-4	Solar Panel Weight and Temperature vs. Heliocentric Distance	2-15
3-1	Cover Glass Thickness vs. Maximum Power Ratio	3-2
3-2	Spectrum of Giant Solar Flare	3-3
3-3	Maximum Solar Cell Panel and Battery Power Available	3-5
3-4	Comparison of Transistor Radiation Damage and Giant Solar Flare Exposure Dose as a Function of Shielding	3-4
4-1	Isotope Power Supply Surface Temperature	4-4
4-2	Solar Heating of RTG	4-6
4-3	Radioisotope Thermoelectric Generator	4-9
4-4	Radioisotope Thermoelectric Power Generators for Space Vehicles	4-10
4-5	Weight of Isotope, Cladding, and Total Heat Source vs. Thermal Power Output for Plutonium Oxide	4-12
4-6	Cladding Thickness vs. Thermal Power Output	4-13
4-7	Weight of Isotope, Cladding, and Total Heat Source vs. Thermal Power Output for Plutonium Nitride	4-14
4-8	Fin Weight vs. Cold-Junction Temperature	4-15
4-9	Component and Total Weight of RTG as a Function of Power	4-16
5-1	Ray Density Between Source and Detector	5-3
5-2	Minimum Weight Optimized Shields as a Function of Position	5-4
5-3	Change of Weight Optimized Shield with Attenuation Factor	5-5
5-4	Comparison of Optimum Shields Calculated With and Without Build-Up Factors	5-6

LIST OF TABLES

<u>Table</u>		<u>Page</u>
1-1	Power Loading Requirements	1-2
2-1	Power Output Degradation Factors	2-12
2-2	Standard Values of Solar Panel Component Weights	2-12
2-3	Solar Panel Sizing for 200-watt Minimum Output from Power Conditioning Equipment	2-13
4-1	Cost/Availability of Isotopic Power Fuels	4-3
6-1	Comparison of Photovoltaic and Isotopic Power Subsystems (200 watts)	6-2

SECTION 1

OBJECTIVES AND REQUIREMENTS

1.1 BACKGROUND

Since WDL has already surveyed a variety of power supply subsystems [Philco, 1963]; the technical objectives of this study have been accomplished more profitably by concentrating upon only the most promising approaches. Subsystems other than the photovoltaic and isotopic-thermoelectric appear to present more problems. For example, the present state of development of thermionic diodes is not as promising as thermoelectric diodes. Solar concentrators require a high degree of pointing accuracy which overshadows the few advantages gained. The Brayton cycle is complex and has moving turbines which are undesirable from reliability and from magnetic field and gyroscopic moment standpoints. Isotopic batteries are inherently high-voltage, low-current generators, and information on them gives little hope for a high-power-output device.

1.2 REQUIREMENTS

Requirements upon the design of the power system are the following:

1. Continuous available d.c. power of 200 to 350 watts, depending on the mission requirements
2. Operation between 1 and 2 A.U. heliocentric distance
3. One-year life

The power loading requirements during various flight phases for continuously operating 10-watt, 25-watt and 50-watt power amplifiers are detailed in Table 1-1.

TABLE 1-1 Power Load Requirements

LAUNCH	PRE-LAUNCH	LAUNCH	ACQUI-SITION	CRUISE	MANEUVER (TWICE)	EN-COUNTER	PLAY-BACK
16	16	16	16	16	16	16	16
7	7	7	7	7	7	7	-
0.2	0.2	0.2	0.2	0.2	0.2	0.2	-
3.5	3.5	3.5	3.5	3.5	3.5	3.5	-
2.0	2.0	2.0	2.0	2.0	2.0	2.0	-
0.5	0.5	0.5	0.5	0.5	0.5	0.5	-
-	-	-	-	-	-	8.0	-
-	-	-	-	-	-	12.0	-
-	-	-	-	-	-	3.0	-
-	-	-	-	-	-	9.0	-
-	-	-	-	-	-	8.0	-
2.1	2.1	2.1	2.1	2.1	2.1	3.0	-
15	15	15	15	15	15	15	15
15	15	15	15	15	15	15	15
3	3	3	3	3	-	3	3
3	3	3	3	3	3	3	3
2	2	2	2	2	2	2	2
3.5	3.5	3.5	3.5	3.5	3.5	3.5	3.5
1.85	1.85	1.85	1.85	1.85	1.85	1.85	1.85
74.65	74.65	74.65	74.65	74.65	71.65	115.55	59.35
83.50	83.50	83.50	83.50	83.50	80.20	129.22	68.90
-	-	-	-	-	-	7	6
-	-	-	-	-	-	9.35	8.00
0.69	0.69	0.69	0.69	0.69	0.69	0.69	0.69
84.19	84.19	84.19	84.19	84.19	80.79	139.26	77.59
105.2	105.2	105.2	105.2	105.2	101.0	176.5	97.0
10.35	10.35	10.35	13.50	6.00	13.5	6.0	6.0
10.35	10.35	10.35	13.50	6.0	54.0	6.0	6.0
24.9	24.9	24.9	32.6	14.48	163.3	14.48	14.48
4.40	4.40	4.40	4.40	20.20	-	-	-
-	28.5	28.5	28.5	28.5	28.5	28.5	23.5
134.5	163.0	170.7	170.7	168.35	266.4	219.48	140.
138.7	168.0	176.0	176.0	173.8	303.5	226.2	144.3

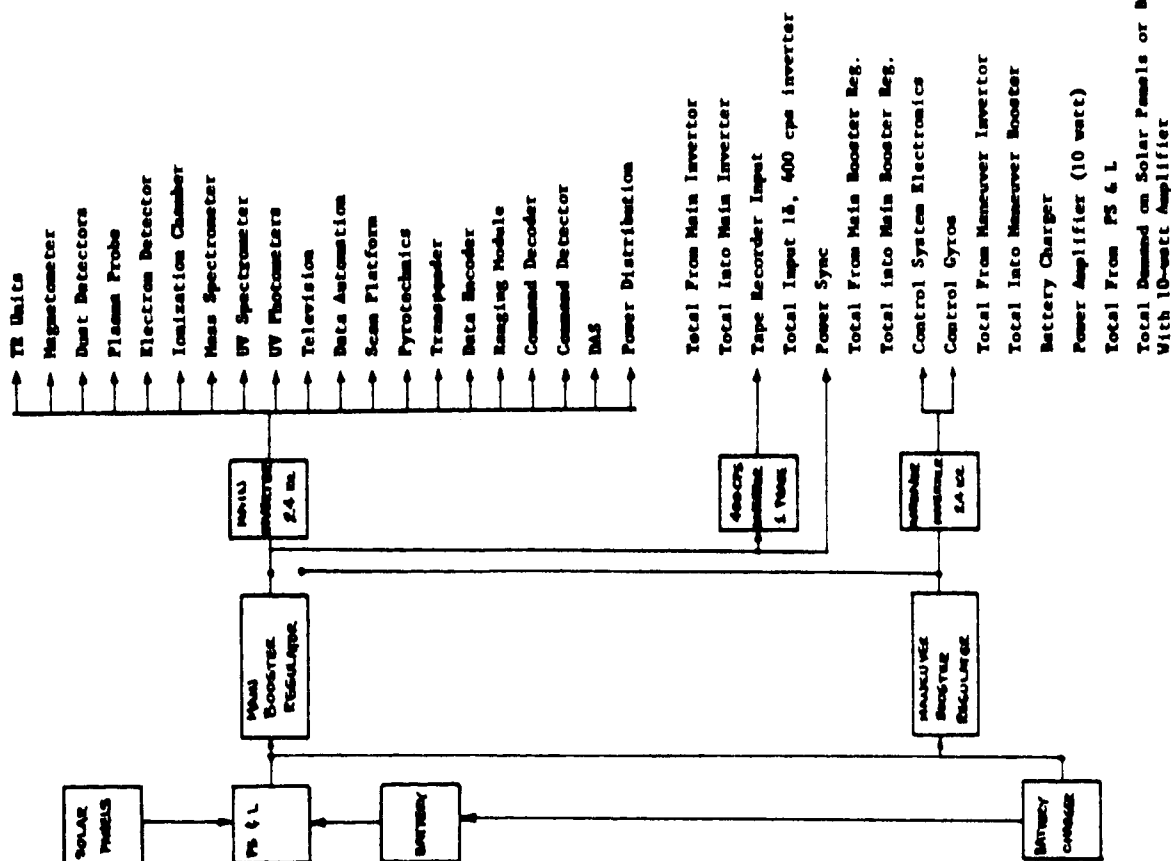


TABLE 1-1 Power Load Requirements
(Continued)

	PRELAUNCH	LAUNCH	ACQUISITION	CRUISE	MANUEVER	ENCOUNTER	PLAYBACK
Total Demand on Solar Panels or Battery With 10-watt Amplifier	138.7	168.0	176.0	173.8	303.5	226.2	144.3
Additional Power Required for 25-watt Output Amplifier	-	46.5	46.5	46.5	46.5	46.5	46.5
Total Demand on Solar Panels or Battery With 25-watt Amplifier	138.7	214.5	222.5	220.3	350.0	272.7	190.8
Additional Power Required for 50-watt Output Amplifier	-	75	75	75	75	75	75
Total Demand On Solar Panels or Battery for Spacecraft With 50-watt Amplifier	138.7	289.5	297.8	295.3	425.0	347.2	265.8

SECTION 2

PHOTOVOLTAIC POWER SUBSYSTEM

2.1 FUNCTIONAL DESCRIPTION

The power subsystem supplies a minimum of 200 watts at 28 volts from power conditioning equipment. A secondary silver-zinc battery system, which is recharged regularly by solar panels, supplies power during acquisition, maneuvers and intervals of peak-power loads, and will also supply power during launch and solar-panel deployment. The photovoltaic power subsystem consists of a series-parallel arrangement of solar cells. The solar cells are mounted flat on four rectangular or trapezoidal panels that are oriented normal to the solar flux. Blocking diodes are connected in each series string, and shunt diodes are placed across each parallel group to minimize losses from open cells and/or shadowing. Solar cells are installed with multi-layer transmission filters deposited on cover slides that are bonded directly to the cell surface by a transparent adhesive. The filter-adhesive-solar cell combination is henceforth referred to as the "cell stack". The following sections discuss the problems associated with cell-stack components and their selection based on present state-of-the-art capabilities.

2.1.1 Solar Cells

The standard size (1 x 2 cm) N-on-P silicon cells with 10 ohm-cm base material resistivity have been selected because of their combined high radiation resistance and high power output. The radiation resistance characteristic is particularly significant because of the uncertainties associated with the space radiation environment. This type of cell is available currently in large quantities from several manufacturers. The minimum performance characteristics under a simulated solar intensity of 140 milliwatts/cm² are shown in Figure 2-1. This bare cell has 10 percent conversion efficiency under air-mass-zero (AMO) conditions at 28°C with an active cell area of 1.9 cm². The 10 percent efficiency represents the current capability of major manufacturers of silicon solar cell available in production quantities.

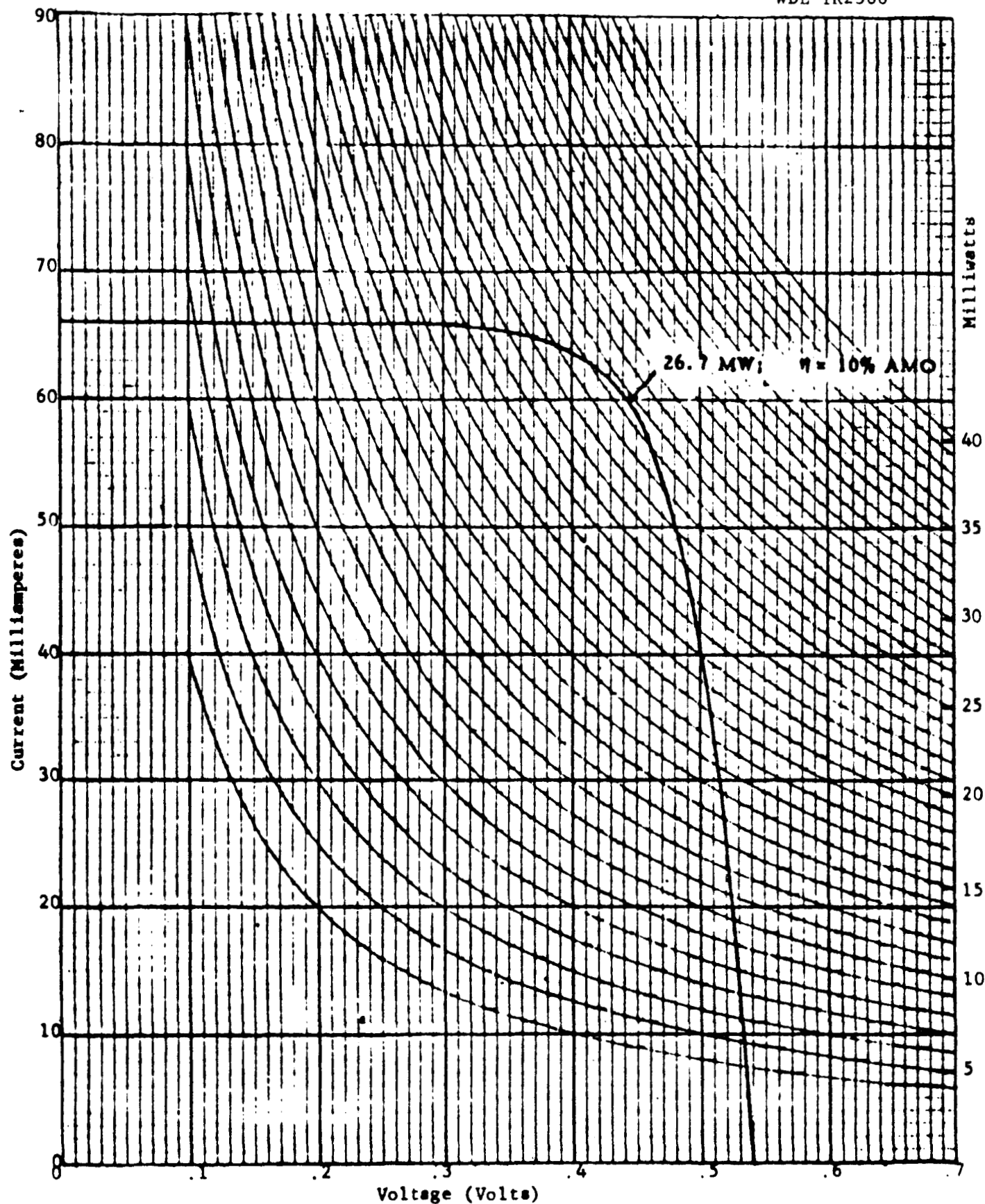


Fig. 2-1 Solar Cell Current - Voltage Characteristics

The best conversion efficiency achieved to date with silicon is 14 percent, while normally production quantity cells are between 8 percent and 12 percent with an approximate gaussian distribution. Future efforts to skew this distribution toward the higher efficiency range will probably result from efforts devoted to forming the junction precisely where it is desired. The theoretical upper efficiency limit with single-crystal silicon solar cells has been calculated by Prince (1955) to be 21.6 percent. However, losses due to surface reflections, incomplete absorption, incomplete collection of electron-hole pairs, partial utilization of photon energy for electron-hole pair creation, and internal series resistance limit the achievable conversion efficiency to 15-16 percent. Large-quantity production further reduces this efficiency by a few percent. Improved manufacturing methods can be expected to reduce costs in the future.

Gallium arsenide solar cells have been eliminated from any consideration beyond that given in the Solar Probe Study [Philco; 1963] because of their premium cost which does not buy any significant operational advantage on comet missions. The GaAs cells are more radiation resistant than silicon; however, a small additional thickness of cover glass over the light~~ten~~ silicon cells would provide equivalent radiation resistance. The silicon solar-cell power output is greater than the GaAs at temperatures below 120°C.

Considerable effort is underway at NASA and under Air Force contracts on thin-film solar-cell development using silicon, gallium arsenide, cadmium sulfide and gallium telluride. Thin-film cells have advantages in weight, panel-design flexibility and possibly radiation resistance. At present, however, only comparatively inefficient thin-film cells have been developed and these have not been made with reproducible characteristics [Shirland, Wolff, Schaefer and Dierssen; 1962]. Data is unavailable on thin-film operating life and storage effects. Polycrystalline cadmium sulfide presents an additional ground handling and spacecraft installation problem since it deteriorates rapidly upon exposure to the atmosphere.

2.1.2 Cover Glass Slides

Cover glass slides are bonded to the solar-cell surface with transparent adhesive. These cover slides provide protection from particle radiation, increase the cell's spectral emittance, and afford micrometeoroid protection. An intensive investigation conducted during the MACS design effort indicates that fused silica suffers the least reduction in transmission after exposure to electrons, protons, and ultraviolet radiation of the materials investigated to date. The solar panel power output is a function of the cover-slide thickness since a significant range of particles is absorbed and high-energy particles, damaging to cells and adhesives, undergo a substantial energy reduction while traversing the cover slide. Thus an increased thickness means fewer cells are required for the desired power. This presents a trade-off situation between the weight penalty incurred by increasing cover slide thickness and the resulting decrease in panel size for 30- and 60-mil thick fused-silica cover slides on six comet missions. If the power output at the design point must be increased, the cover thickness can be increased.

2.1.3 Optical Filter

A multi-layer interference filter is vacuum-deposited on the inner surface of the cover glass and an anti-reflective coating deposited on the outer surface, i.e., exposed surface. A transmission cut-on wavelength of 435 millimicrons is recommended for this filter. This cut-on can provide better protection against transmission losses in the adhesive due to ultraviolet degradation, while paying a very small penalty in power for cutting off a small portion of the cell's spectral response. The cut-on selection is conservative but justified at this time, since test data is scarce on ultraviolet degradation, degradation of filters and adhesives, and since current testing procedures indicate substantial uncertainties. Further testing and adhesive R&D work may optimize the filter characteristics.

2.1.4 Solar-Cell Cover Transmissive Adhesive

Space environmental effects on the mechanical properties of adhesives are not significant in solar cell applications. This is because cover slide materials are relatively impermeable to gases, and outgassing of volatile products in the adhesive can occur only through the very small exposed area at the edges of the adhesive bond line. Studies have indicated that this is an extremely slow process even with the accelerated rate of volatilization due to vacuum radiation and high temperatures. The primary considerations for solar-cell cover adhesives are their transmission and absorptance characteristics. These adhesives are quite susceptible to ultraviolet degradation. However, the blue filter reflects the bulk of the energy below 0.435 micron and minimizes the transmission loss.

2.1.5 Ultraviolet Exposure Degradation

Little is known about the chemical degradation process associated with the ultraviolet and particle-radiation exposure of transmissive adhesives. Current environmental ultraviolet-radiation testing employs either Mercury arc or Xenon lamps. These sources do not match the solar ultraviolet spectral distribution. Disparities associated with the correlation of flight data and test results indicate that large uncertainties must be assigned to present data. Mariner 2 flight data indicate that the transmittance of the LTV-602 solar-cell cover adhesive was not adversely affected during its mission [Zontendyk, Vondra and Smith, 1963]. Several promising silicon-base transparent adhesives are being investigated at WDL and elsewhere under simulated space conditions to determine transmission degradation effects resulting from particle and ultraviolet exposure. A degree of skepticism should be applied to simulated testing with current techniques. Flight tests of more promising silicon-based adhesives are recommended, coupled with a critical evaluation of the instrumentation employed.

Ultraviolet degradation of thermal control materials results in an increased thermal absorptance. This increase in thermal absorptance is a non-linear temperature phenomenon that diminishes with lower

temperatures. Samples of rutile titanium-dioxide pigment in a silicon binder flown aboard OSO-I indicate a very small increased thermal absorptance at temperatures well above those calculated for comet missions. The rear panel surface has a negligible view factor of the spacecraft; consequently it should not be affected by ultraviolet exposure.

2.1.6 Solar Array Wiring

In order to minimize magnetic effects of current loops within the array, the photovoltaic circuits should be backwired. Backwiring involves bringing the return wire from a group of cells along the center of the back of that group to a point where the two wires can be made a twisted pair. Thus, for every current in a group of illuminated solar cells, an equal and opposite current returns down the back of the group, and the net current flow is zero. Failure of separate modules will thus not distort the gross patterns of current flow in the solar cell surfaces.

2.2 PHOTOVOLTAIC PANEL DESIGN

2.2.1 Cell Stack Temperature

Panel sizing has been based on the current-voltage characteristic temperature dependence of a N/P silicon cell with a manufacturer's conversion efficiency rating of 10 percent. Perihelions of the comets of interest have been used as the design position for minimum power output. The most important panel sizing parameter is the solar-cell stack temperature from panel deployment to post-intercept. The solar panel temperature profile as a function of position with respect to the sun has been determined using two control-volume boundaries. The first considers the active solar cell surface, the uncovered frontal thermal surface, and the conductive panel substrate up to, but not including, the rear panel thermal control surface. The energy balance for this system is as follows:

$$\sigma T_f^4 [e_{sc} Z + e_f (1 - Z)] + \frac{T_f - T_b}{R} + \frac{P}{A} - S \cos \theta [Z \tau \alpha_{sc} + (1 - Z) \alpha_f] = 0 \quad (2-1)$$

The second considers the heat transferred by non-ideal conduction and the rear panel emitting surface:

$$\frac{(T_f - T_b)}{R} + \sigma \epsilon_b T_b^4 = 0, \quad (2-2)$$

where

- A = total panel surface area
- P = power from solar cell conversion
- R = equivalent thermal resistance of panel substrate
- S = incident solar flux
- T = absolute temperature
- Z = packing factor
- σ = Stefan-Boltzmann constant
- ϵ = emissivity
- α = absorptance
- θ = off-normal angle between panel surface and incident solar flux
- τ = transmission through filter and adhesive,

and the subscripts are defined as follows:

- f = panel front surface (not covered with solar cells)
- b = panel rear surface
- sc = solar cell-adhesive-filter composite

An equivalent thermal resistance accounting for non-ideal panel conduction has been determined with Mariner 2 flight data. The following thermal control surface materials were considered in this determination:

<u>Surface</u>	<u>Material</u>	<u>Condition</u>	<u>α</u>	<u>ϵ at 285°K</u>
Rear panel	Silicon Acrylic	ZnS Pigmented	0.30	0.91
Inactive Front Panel	Silicon Alkyd	Rutile Pigmented	0.12	0.89
Filter-Cell-Adhesive	Combination	Rutile Pigmented	0.80	0.83

2.2.2 Cover Glass Slides

Cover glass slides are bonded to the solar-cell surface with transparent adhesive. These cover slides provide protection from particle radiation, increase the cell's spectral emittance, and afford micrometer-or-oid protection. Investigation indicates that fused silica suffers the least reduction in transmission after exposure to electrons, protons, and ultraviolet radiation of the materials investigated to date [STL, 1964]. The solar panel power output is a function of the cover-slide thickness since a significant range of particles is absorbed and high-energy particles, damaging to cells and adhesives, undergo a substantial energy reduction while traversing the cover slide. Thus an increased thickness means that fewer cells are required to the desired power. This presents a trade-off situation between the weight penalty incurred through additional cover-slide thickness and the resulting decrease in panel size for 30- and 60-mil thick fused-silica cover slides. If the power output at the design point must be increased, the cover thickness can be increased.

2.2.3 Optical Filter

The solar cell optical filter consists of a series of optical quarter-wavelength thick dielectric coatings vapor deposited on the surface of the cover glass which mates with the solar cell's surface. An anti-reflective coating, usually MgF_2 , is deposited on the opposite surface, which is the one that the incident solar flux first encounters. These optical filters reflect portions of the solar energy spectrum outside the region of the cell's spectral response, which is 0.40 to 1.2 microns for silicon cells. The energy transmitted to the cell outside this bandwidth contributes only to heating. This heat is undesirable because the cell's conversion efficiency is inversely proportional to the cell's temperature.

The term "blue filter" describes the filter which reflects incident solar flux at wavelengths lower than the cell's initial response wavelength, i.e., it rejects the ultraviolet portion of the solar spectrum.

A blue-red filter is made by vapor depositing additional dielectric film layers on the basic blue filter such that it will also reject transmission in the infra-red region. Preliminary calculations for the Pons-Winnecke mission indicate an appropriate power gain of 2 percent could be realized if blue-red filters were used. The power gain would be less for comet missions with intercepts at higher AU distances from the Sun. Current costs of blue-red filters are almost three times that of blue filters. This additional cost is not considered justifiable for the small power gain achieved. Further calculations in this study are all based on the blue filter characteristics.

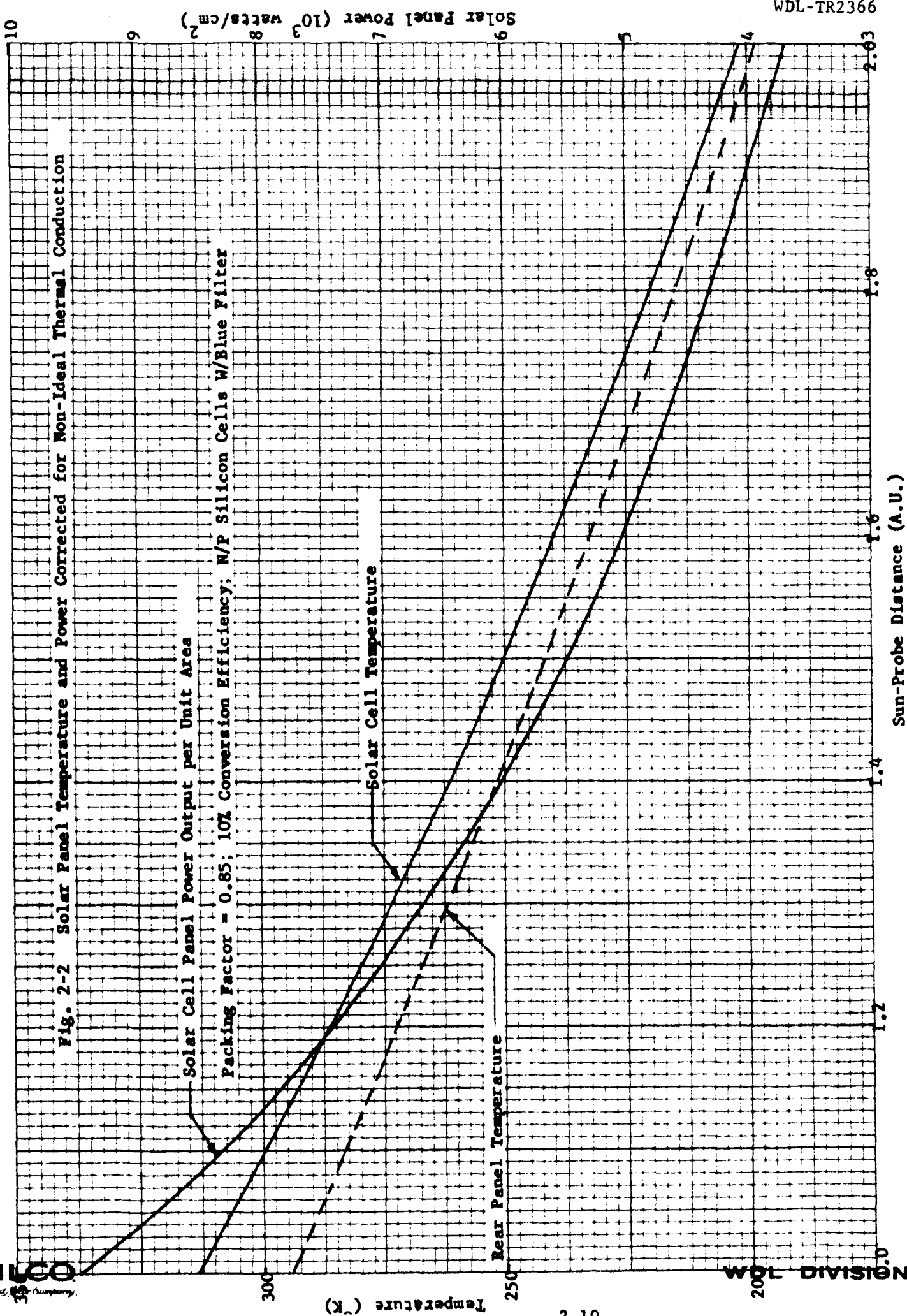
A transmission cut-on wavelength of 435 millimicrons is recommended for the blue filter. This cut-on can provide better protection against transmission losses in the adhesive due to ultraviolet degradation, while paying a very small penalty in power for cutting off a small portion of the cell's spectral response. The cut-on selection is conservative but justified at this time, since test data is scarce on ultraviolet degradation, degradation of filters and adhesives and current testing procedures indicate substantial uncertainties. Further testing and adhesive R&D work may optimize the filter characteristics.

The emissivity values used in the calculations have been temperature corrected for non-ideal thermal conductions. Figure 2-2 represents the solar-cell and rear-panel surface temperatures calculated by trial and error over the range of heliocentric distances at intercept. The power output per unit area of panel is determined as follows:

$$P/A = SZ\eta_{sc}\eta_T\eta_B \quad (2-3)$$

where

Fig. 2-2 Solar Panel Temperature and Power Corrected for Non-Ideal Thermal Conduction



P/A = panel power output per unit area

S = incident solar flux

(The solar constant varies throughout the year from 144.8 to 135 milliwatts/cm². The minimum value has been used.)

Z = packing factor = 0.85

η_{sc} = 0.095 for N/P silicon cells rated at 10% efficiency with an active cell area of 1.9 cm² in a 2.0 cm² cell area having the grid wires parallel to the long dimension

η_T = cell temperature efficiency dependence

$$= 1 - (4.7 \times 10^{-3})(T - 301^\circ K)$$

η_B = ratio of filtered efficiency to bare-cell efficiency

$$= \frac{\int_{\lambda_1}^{\lambda_2} \tau(\lambda) S(\lambda) R(\lambda) d\lambda}{\int_0^{\infty} S(\lambda) R(\lambda) d\lambda} \cong 0.92 \text{ with blue filter}$$

$R(\lambda)$ = cell spectral response

$S(\lambda)$ = solar energy spectral distribution

$\tau(\lambda)$ = spectral transmittance through filter and adhesive.

The solar panel power output per unit area as a function of distance from the sun is shown also in Figure 2-2.

2.2.4 Panel Sizing

Calculations have been performed to determine a solar array design capable of providing 200-watts output power at 28 volts from power conditioning equipment for a one-year mission to comets at distances from the sun equal to those at intercept. The major considerations in sizing the array and in calculating performance are summarized in Tables 2-1 and 2-2. Table 2-3 summarizes the panel size and weight calculations based on all factors discussed.

TABLE 2-1

POWER OUTPUT DEGRADATION FACTORS

N/P Silicon Solar-Cell Array	Efficiency Factor
Diode and wiring	0.95
Random open circuit	0.94
Ultraviolet adhesive transmission	0.97
Panel: solar flux $\pm 1^\circ$ off normal orientation	Negligible
Radiation of Giant Solar Flare	
30-mil cover glass	0.696
60-mil cover glass	0.773
Micrometeorite erosion on cover glass	0.98
Operation at other than maximum power point	0.95
Cell mismatch	Negligible
Overall Efficiency - 30 mil : 0.563 - 60 mil : 0.623	

TABLE 2-2

STANDARD VALUES OF SOLAR PANEL COMPONENT WEIGHTS

Component	Weight (lb/ft ²)
Solar Cells	0.28
Adhesive (typical)	0.15
Cell Interconnecting Wiring	0.02
Fused-Silica Cover-Glass with Filter	
30-mil thickness	0.34
60-mil thickness	0.68
Panel without Cells Including Structure	0.61
Total Panel Weight with Cells and	
30-mil cover glass	1.30
60-mil cover glass	1.59
(Packing Factor = 0.85)	

TABLE 2-3

SOLAR PANEL SIZING FOR 200-WATT MINIMUM OUTPUT
FROM POWER CONDITIONING EQUIPMENT

Comet	Maximum Encounter Distance (AU)**	Cover Glass Thickness (mils)	Temp. °K	P/A 10 ³ watts/cm ²	Total Panel Area* (ft ²)	Total Panel Weight (lbs)
Brooks (2)	1.80	30 60	220	4.29	90.6 80.4	113.2
Pons-Winnecke	1.26	30 60	278	6.96	54.9 49.2	68.6 78.3
Tempel (2)	1.36	30 60	266	6.60	57.9 51.9	72.3 82.6
Kopff	1.57	30 60	243	5.19	74.3 66.0	92.9 105.0

* Packing Factor = 0.85

**Heliocentric

Figure 2-3 shows the total panel area as a function of heliocentric distance at encounter, the output power desired, and the cover glass thickness. The panel temperature is also shown. Figure 2-4 shows the corresponding solar panel weight for the same parameters.

2.3 BATTERIES

Rechargeable batteries supply power during prelaunch, launch, solar panel deployment and initial sun acquisition. These batteries also supply power during reacquisition and maneuver, peak power loads and the playback of stored data during post-intercept. Self-sealed, rechargeable silver-zinc batteries have been chosen on the basis of the following factors:

1. High ratio of output power to unit weight and volume compared with other alkaline electrolytic batteries.

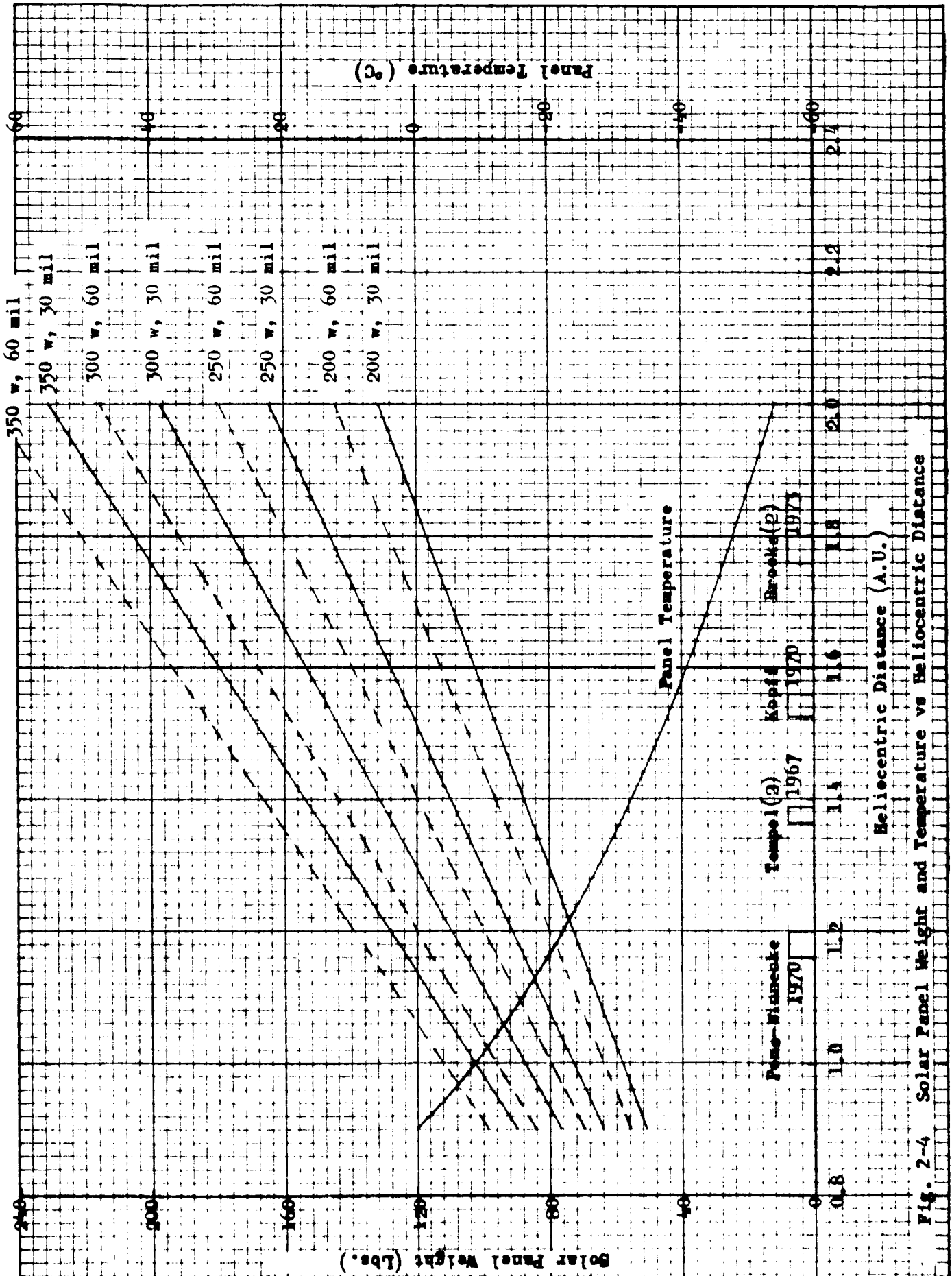


Fig. 2-4 Solar Panel Weight and Temperature vs Heliocentric Distance

2. Constant voltage characteristic during discharge at high power output levels.
3. Operation over wide range of temperatures.
4. Discharge at both high and low rates.
5. Mechanically rugged.

Since magnetic field measurements are to be taken on the Comet missions, components with minimum magnetic effects are required. However, the present location of the magnetometer on the boom and remote from the battery location probably negates any magnetic effects from the silver-zinc battery. Silver-cadmium batteries are non-magnetic and could be used if an magnetic effects analysis indicates interference with the scientific instrumentation.

A silver-zinc secondary battery system similar to the design for Mariner Mars has been used for preliminary design study purposes. This system has a 1200 watt-hour maximum rating. The load requirement varies between 0 and 9.5 amps with a voltage regulation between 25.8 and 33.3 volts. This battery and case weighs about 37.5 pounds. The choice of a sealed or vented-cell battery with a pressurized canister should reflect the results of current developmental programs. The sealed cell is more sensitive to overcharge and presents a potential explosive hazard. The vented cell also has disadvantages in a vacuum.

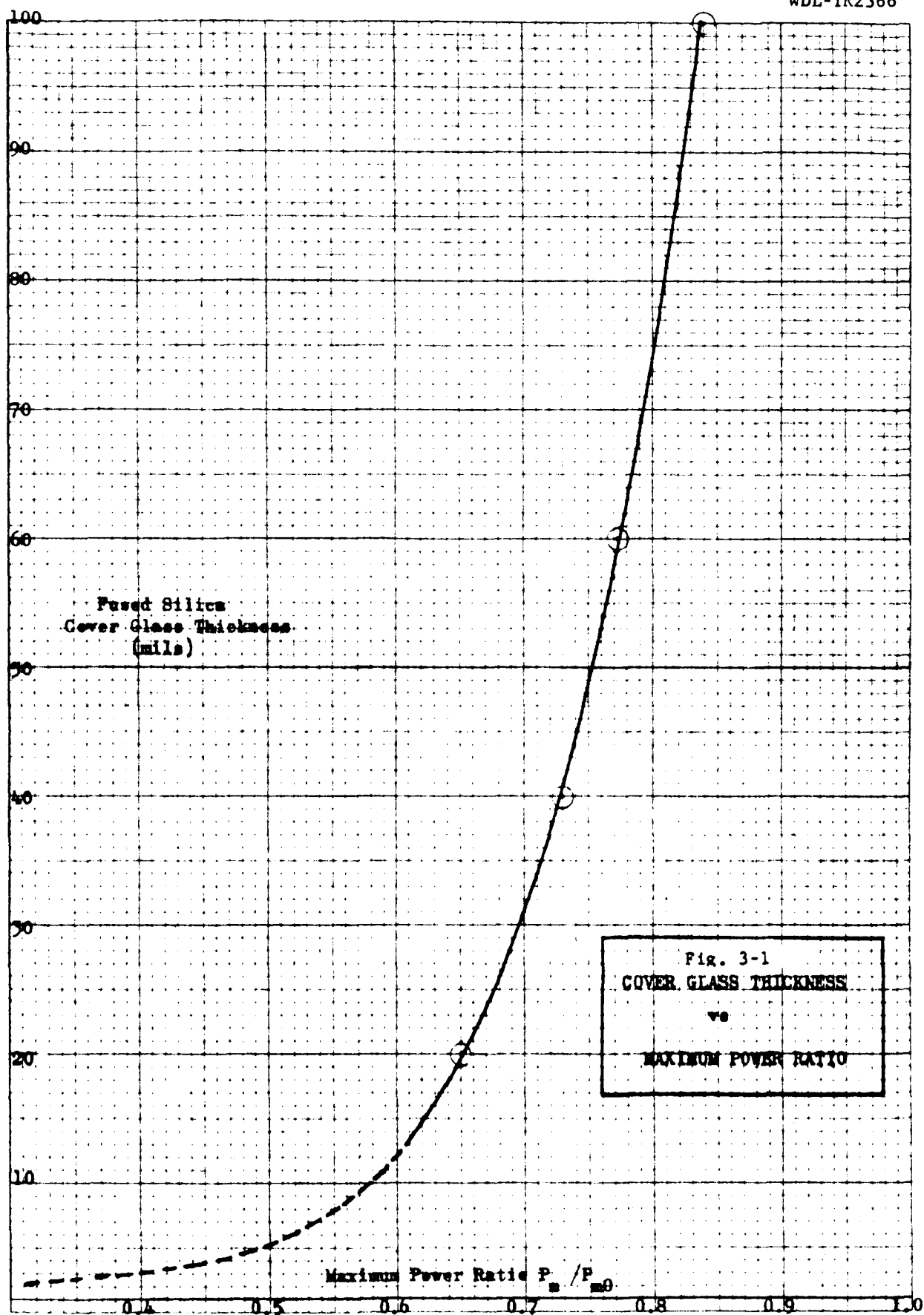


Figure 3-3 indicates the solar panel output power degradation after a giant solar flare and the resulting maximum battery output power required during a 24-hour period. The calculations were made for 100 sq. ft. of panel area, the maximum area accommodated by the Surveyor shroud.

3.2 DAMAGE IN ELECTRONICS

A preliminary study of proton doses inside spacecraft indicates that high-quality transistors can survive a giant solar flare. Even considering the largest event that ever occurred, the 14 July 1959 giant flare [Singer, 1964], it appears that internal doses are below the estimated threshold for severe damage [Battelle, 1963] to high-quality transistors. With less than 250 mils of aluminum shielding, the internal dose is greater than the external dose due to secondary nuclear reactions [Singer, 1964].

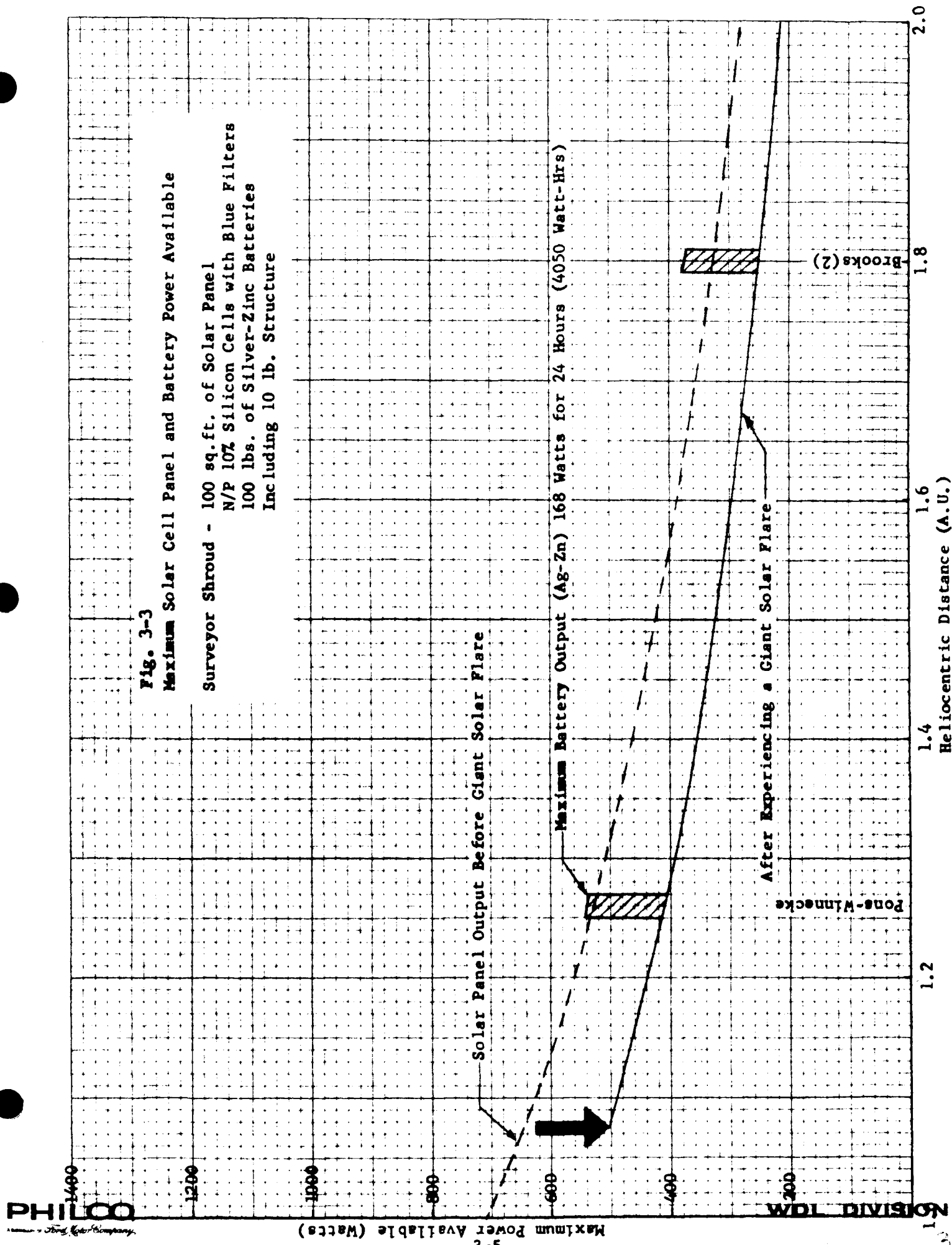
3.2.1 Calculations

The radiation threshold for transistors has been established as within the range of 10^{10} to 10^{12} p-cm⁻² [Battelle, 1963]. This threshold appears realistic since experimental research has shown that pronounced changes occurred for exposure to 10^{12} to 10^{13} p-cm⁻² of 22 Mev protons and 10^{11} to 10^{12} p-cm⁻² of 240 Mev protons. Some variation between radiation tolerance of high- and low-frequency transistors can be expected because of the greater resistance to damage shown for thin-base elements. Some experiments have been conducted in which all important transistor characteristics changed drastically, with the exception of the rectifying properties.

The particle doses given in the Battelle summary have been converted to exposure doses by the following formula:

$$\text{Exposure Dose} = N \bar{E} (0.69) (1.6 \times 10^{-6}) 10^{-2} \text{ rads (C)}$$

where N = the number of particles encountered by omnidirectional spherical detector, \bar{E} = the average energy of particles in Mev, and 0.69 is the ratio of surface areas of a 1 gram sphere of carbon to a spherical detector of 1 square centimeter cross section. These are plotted as bar graphs in Figure 3-4. Also indicated are the proton doses from giant flares as published in



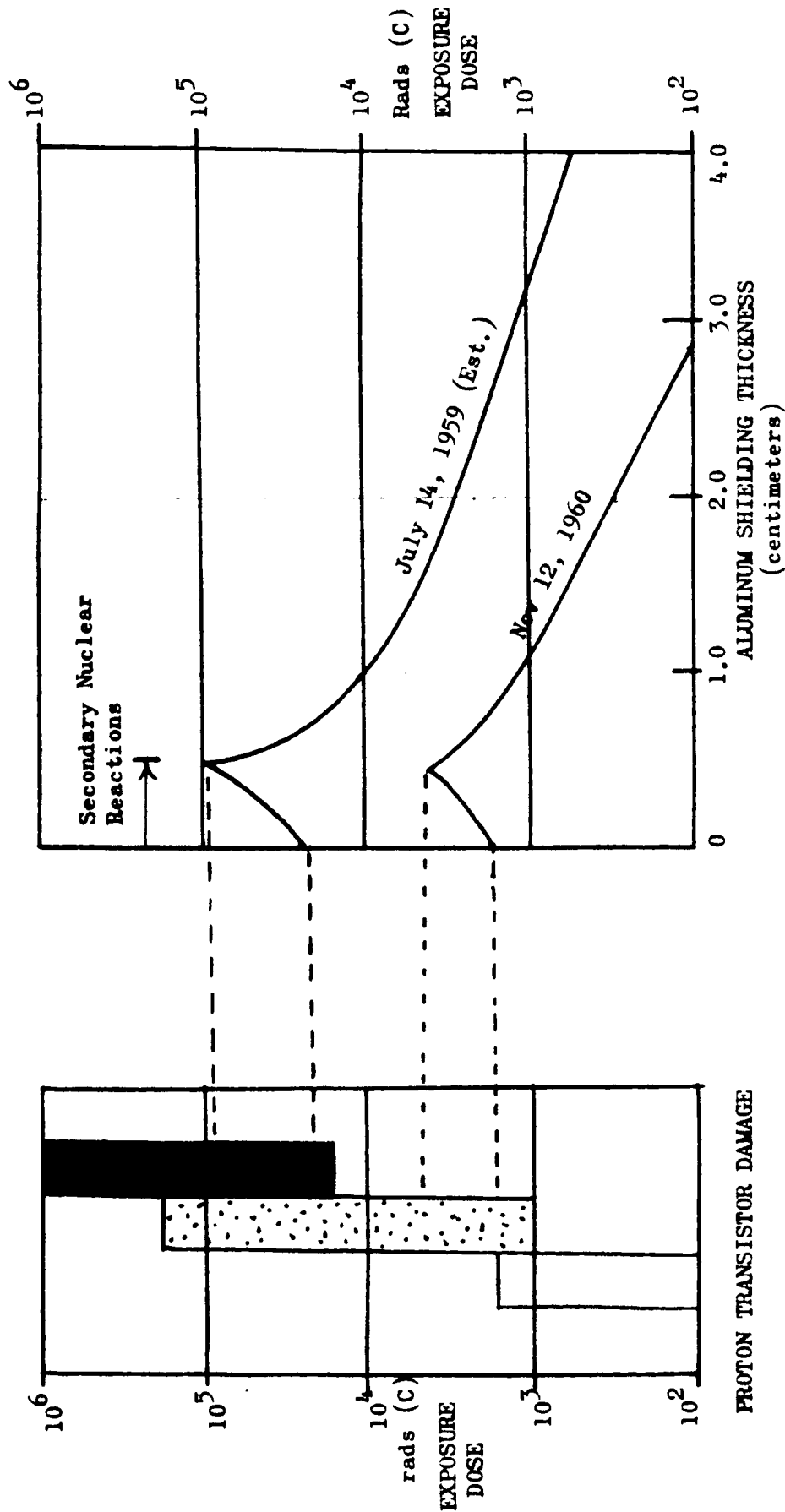


Fig. 3-4 COMPARISON OF TRANSISTOR RADIATION DAMAGE AND GIANT SOLAR FLARE EXPOSURE DOSE AS A FUNCTION OF SHIELDING

[] Mild or No Effect
 [] Moderate Damage; Degradation
 [] Severe Damage, Inoperable

the recent Singer article. Data on the November 12, 1960 giant flare is the best available; it is a combination [Masley and Goedeke, 1962] of satellite data from Discoverer XVII and Explorer VII, three NASA rockets, balloons, and riometer data. The July 14, 1959 event was not so well covered, and values used here are estimations by Singer.

3.2.2 Evaluation

The study of solar flare damage to spacecraft electronics cannot be considered closed on the basis of this preliminary study. The question of secondary nuclear reactions as presented in the references used here is still considered doubtful.

SECTION 4

ISOTOPIC POWER SUBSYSTEM

4.1 THERMOELECTRIC TECHNOLOGY

Radioisotope-thermoelectric generators (RTG) have been operated at efficiencies of 2 to 8 percent using semiconductor thermoelectric materials such as germanium silicide (GeSi). Three other approaches have been examined, and the possibility of increasing efficiencies up to 15 percent may be feasible in the future.

4.1.1 Segmented Bismuth Telluride - Lead Telluride Modules

Several development programs are under way, notably at M.M.M. and Battelle, to fabricate reliable segmented Bi_2Te_3 - PbTe elements. This combination requires a low-temperature cold junction ($T_C = 160^\circ\text{F}$) and appears to be able to give efficiencies around 10 percent. The operating temperatures ($T_H = 960^\circ\text{F}$) are within materials capabilities, but a higher radiator weight will be required to obtain the lower cold junction temperature.

4.1.2 Segmented Lead Telluride - Germanium Silicide

Conversion efficiencies are around 10 percent, but development is still required to produce modules. Cold junction temperatures, $T_C = 350^\circ\text{F}$; hot junction temperature, $T_H = 1280^\circ\text{F}$, which means lower radiator weight.

4.1.3 Multiple-Segmented Modules

This group includes three or more phases, such as Bi_2Te_3 - PbTe - GeSi , or other bonded combinations of segmented modules and single-phase elements. These advanced combinations have been discussed with estimates

of conversion efficiencies up to 15 percent. The approach is to take full advantage of the temperature gradient between hot and cold junction by placing each module between optimum temperatures.

4.2 FUEL AVAILABILITY

Table 4-1 is included as a guide to the most recent information on prices and availability. It is adapted from a rough draft published by Hanford Isotope Plant (HIP) [1964]. Note changes in availability of Curium-244 since the Solar Probe Study, with 1972 prices estimated at \$1500 - 2000/gm.

4.3 COLD-JUNCTION TEMPERATURE

For the purpose of estimating the range of solar degradation of cold-junction temperatures, it has been assumed that the RTG is a right circular cylinder with length equal to diameter. It is reasonable also to assume that the dimensions will be very close to the final design version of Philco's Solar Probe RTG ($L = D = 10''$). This version produced 150 electrical watts with a converter efficiency of 5.8 to 6 percent, and it appears that with slightly higher efficiency thermocouples an RTG producing 200 watts will not increase its dimensions significantly. Four radiation fins are attached parallel to the cylinder axis with dimensions of 10 x 4.35 inches. Estimates have been made of the surface temperature when one end of the RTG faces the sun. To simplify the initial calculations the following assumptions have been made:

- a. Conduction through the support structure is negligible
- b. Surface temperature of cylinder and fins is uniform
- c. The RTG generates 3000 thermal watts continuously
- d. The entire outer surface radiates to space at 0°R and this surface (including fins) is assumed not to "see" any other part of itself or the vehicle.

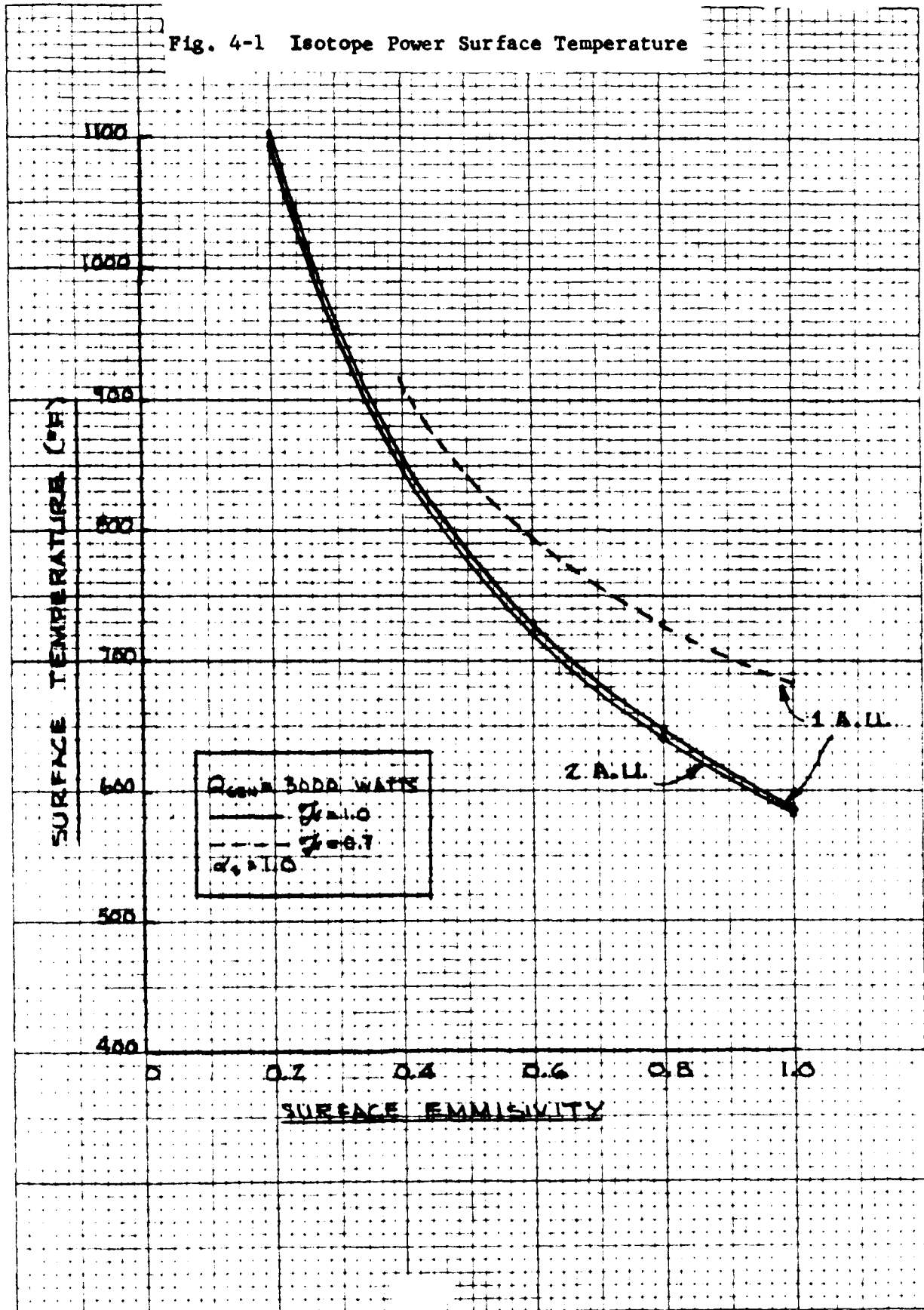
Figure 4-1 shows surface temperature vs. surface emissivity. For $\bar{F} = 1$ and the total interchange factor, $\mathcal{F} = 1$, curves are shown for 1 and

TABLE 4-1

COST/AVAILABILITY OF ISOTOPIC POWER FUELS									
Raw Material	ANNUAL PRODUCTION				COST			AEC Action Req'd for Expanded Capacity	Justification Required by AEC to Initiate Action
	Present	Planned	Potential Capacity	Present	Planned	With Expanded Capacity			
SR-90 Titanate	3,000,000 curies	5,000,000 curies	> 10 megacuries	\$ 3.00/c	\$ 1.00/c	\$20.00/w	\$0.13/c	Construct Manford Isotope Plant (HIP) at AEC Manford Oper. to process fission product waste.	HIP Program presently under study by AEC and announcement of decision by Commission to seek proposals issued.
Cs-137 Glass	1,000,000 curies	3,500,000 curies	> 10 megacuries	2.00/c	0.75/c	21.00/w	0.10/c	See AEC Rpt. MW-77770 for details of HIP Eng. Study. If authorized, HIP could start operations in Jan. 1968.	
Ce-144 Oxide	As needed	3,500,000 curies	> 100 megacuries	0.50/c	0.50/c	0.92/w	0.007/c		
Pm-147 Oxide	> 300,000 curies	500,000 curies	> 30 megacuries	1.00/c	1.00/c	86.00/w	0.033/c		
Pu-238 Metal	4,000 g	10,000 g (1965)	10,000 - 40,000 g	500.00/g	500.00/g	1,000/w	500/g	Five-year lead time for 40 kg/yr.	HIP official request for increased production.
Am-244 Oxide	200 g	1,550 g	Many kg	----	10,000/g	1,000/w	1,500 to 2,000/g	Six-year lead time for first batch. Large capital investment (included in price)	HIP official request for increased production.
Am-242 Oxide	100 g	----	(1967)>1,000 g	12,700/g	----	150/w	12,700/g		
Po-210 Metal	50 g	300-500 g	1,000-10,000 g	>12,700/g	----	~50/w	2,000 to 5,000/g	Modification to plant. \$1.5 M - \$4.5 M (included in price). Two-year lead time for irradiation & construct.	HIP official request for increased production.
Co-60 Metal	Very large capacity. Depends on req't.	----	Very large megacurie	0.50/c	----	----	<0.25/c	One-year lead time or more, depending on quantity.	HIP official request for increased production.

Note: c = curie
g = gram
w = watt

Fig. 4-1 Isotope Power Surface Temperature



2 A.U. To bound the problem, \bar{F} is set to 0.7 and the calculation is repeated for 1 A.U. This curve demonstrates that the RTG will experience no detrimental effect by facing the sun at one end.

Finally, an estimate has been made for the situation when maximum solar flux is incident on maximum RTG area. This is the configuration when the side of the cylinder and two fin faces point at the sun. The increase in temperature resulting from an increase of the ratio of end area to maximum area (1.3/0.545), for a total interchange factor equal to 0.7, is less than 8°F. Figure 4-2 presents an estimate of heating due to solar flux incident at one end. It assumes an absorptivity of 0.3 and is plotted as a function of heliocentric distance.

4.4 RTG DESIGN

The design and integration of a radioisotope thermoelectric generator (RTG) into the comet probe vehicle requires three parallel phases:

- (1) Design of the RTG unit to provide 29 vdc $\pm 1\%$ from 0 to 200 watts (0 to 6.9 amperes).
- (2) Design and compatible placement of required instrument shielding.
- (3) Determination of radiation sensitivity of instrumentation.

The design of an RTG has been completed. The determination of instrument radiation sensitivity and tolerance cannot be made precisely without actual irradiation experiments. The span of ranges lies within 10^{-1} to 10^{10} photons/cm²-sec. These limits are based, respectively, on a gamma-ray detector and on the threshold for semiconductor bulk-damage effects.

The development of a new design technique to produce minimum-weight shielding for spacecraft has been the prime activity of the isotopic power study. A mathematical method based on the calculus of

variations has been developed to derive an optimum shield shape for a given source-detector configuration. The method allows the radiation dose to be prescribed initially (at a particular instrument) and proceeds to develop the equations for the outline of a shield that minimizes the weight of the shield. Multiple-gamma scattering effects are included by incorporating a shield "buildup factor" in the dose integral.

4.4.1 Radioisotope Thermoelectric Generator

The generator is an all-brazed assembly in which all thermoelements are metallurgically joined directly to the heat source and sink. The fuel capsule is a minimum-area right circular cylinder fabricated of Hastelloy C and lined with tantalum for long-term corrosion protection. The capsule is designed to withstand booster fires and earth impact at terminal velocity. A void volume equal to the volume of the fuel is provided in the case of plutonium oxide for containment of the helium gas generated by the alpha decay of plutonium.

A high-temperature fibrous insulating material, Min-K-2000, is machined to fit between the fuel capsule and casing around the thermoelectric modules. The case and four radiator fins are made either of HM21A magnesium-thorium alloy or of beryllium. The density of these materials is approximately the same. The outer diameter of a PuO_2 RTG producing 200 electrical watts is 6.7 inches, with each of the rectangular cross section fins extending 16 inches beyond the casing. The width of the fins is 9 inches; thus they extend approximately one inch beyond the height of the RTG cylinder on top and bottom. Triangular cross-section fins would result in somewhat lighter but longer panels. There is clearance in the Centaur shroud for fins up to 24 inches in length.

The output from the thermoelements, which are connected in series and parallel for optimum voltage-current characteristics, is fed into a power conditioning unit. The load can be varied from no-load

to full-load as required, without regard to damaging the generator. Figure 4-3 shows the current conceptual design of the Philco Comet Probe RTG. Appendix B (classified) shows an alternative rectangular configuration design submitted to WDL by the Martin Company Nuclear Division in response to WDL's Comet Probe solicitation. The resulting dimensions of the 200-electrical watt generator are 23" x 28" x 15" as shown in Figure 3 of the appendix.

Figure 4-4 is a projection of RTG technology to 1971. Many developments are foreseen which will improve the performance of future isotopic generators, thereby producing higher power-to-weight ratios. Currently we are undergoing a transition from PbTe to GeSi thermocouples. PbTe is attacked rapidly by oxygen and is limited to lower temperatures, hence the lower Carnot efficiency and larger radiating fins. GeSi is very stable, has a low vapor pressure and is believed capable of operating at temperatures in excess of 1800° F in a vacuum. The material is quite strong and possesses a low density (3.32 gm/cc). Even higher thermoelectric efficiency can be achieved by using segmented thermoelements. This efficiency is a function of the Carnot efficiency and the material figure of merit. To achieve optimum thermoelectric efficiency, the average figure of merit throughout the chosen temperature range must be a maximum. Since neither material possesses a high figure of merit over the total temperature range produced between fuel capsule and radiation heat sink, an element composed of two (or more) materials with their interface at the temperature of the intersection point of the figure-of-merit curves will achieve maximum efficiency. Segmenting elements in this fashion is not a new concept, but it has not been developed or placed in application in the past due to electrical contact resistance problems. Martin estimates that by 1975, generator power-to-weight ratios will be greater than 5 watts per pound. This will be achieved through improved thermoelectric materials and bonding, fuel processing, and fuel encapsulation.

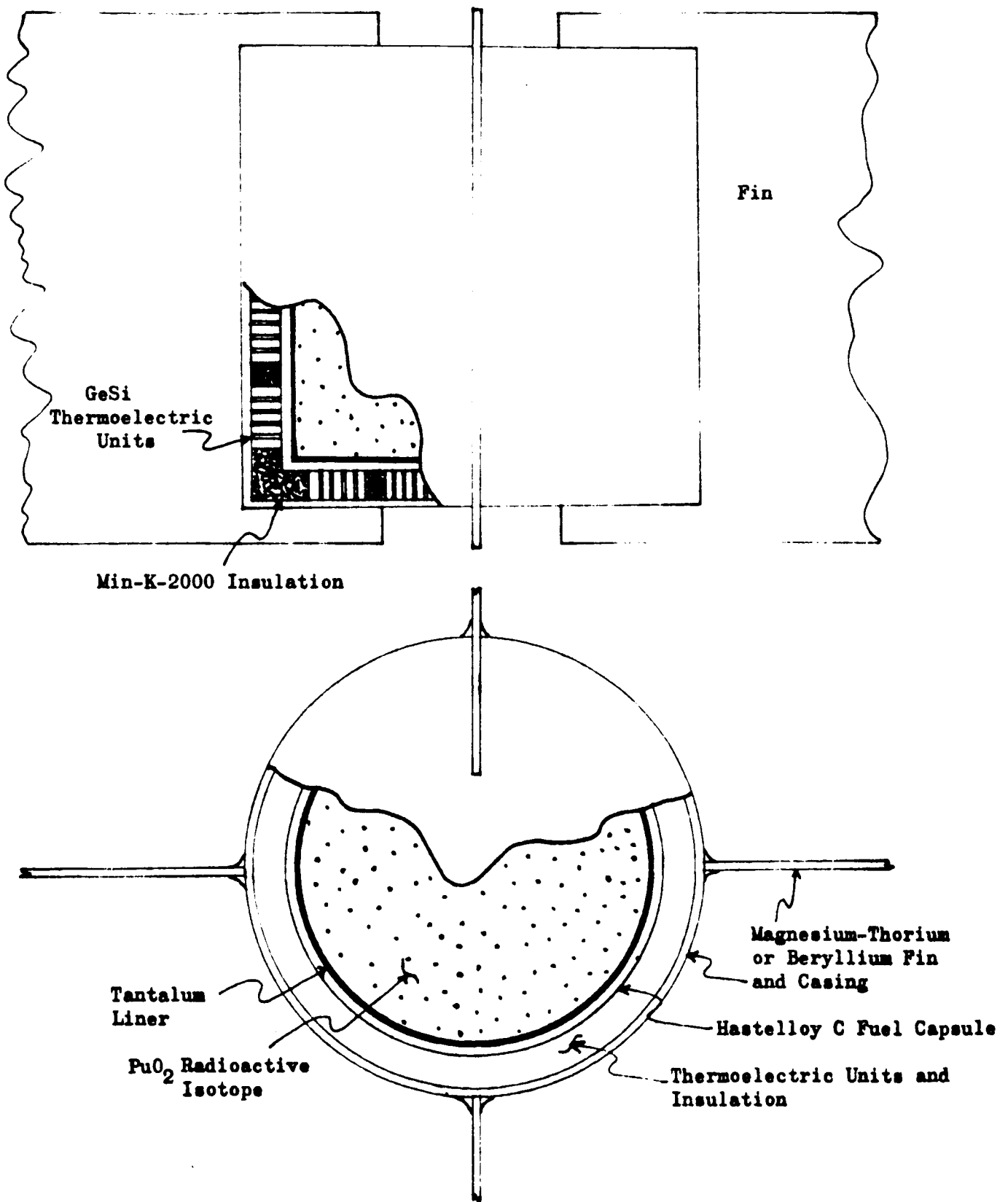
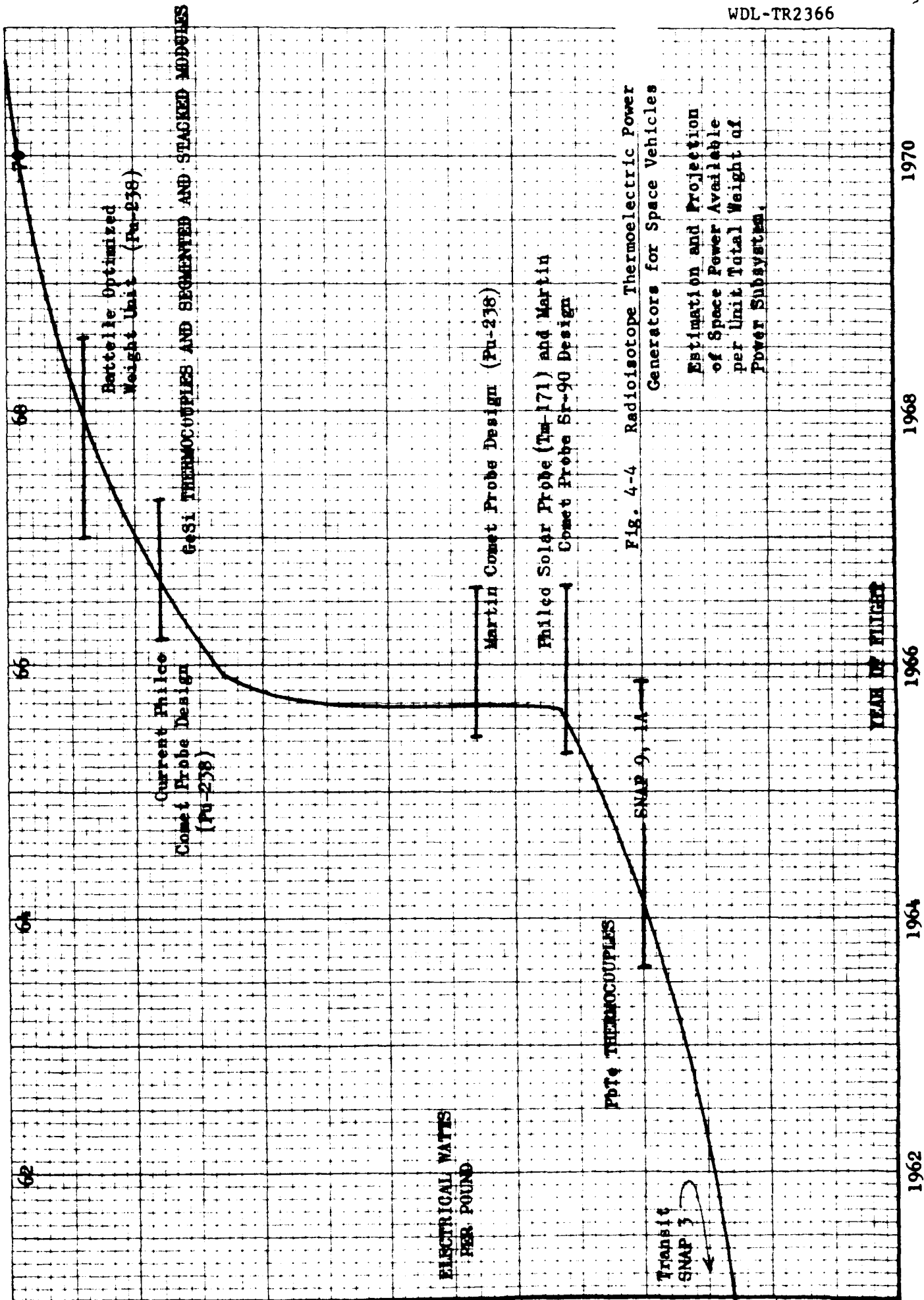


Fig. 4-3 Radioisotope Thermoelectric Generator

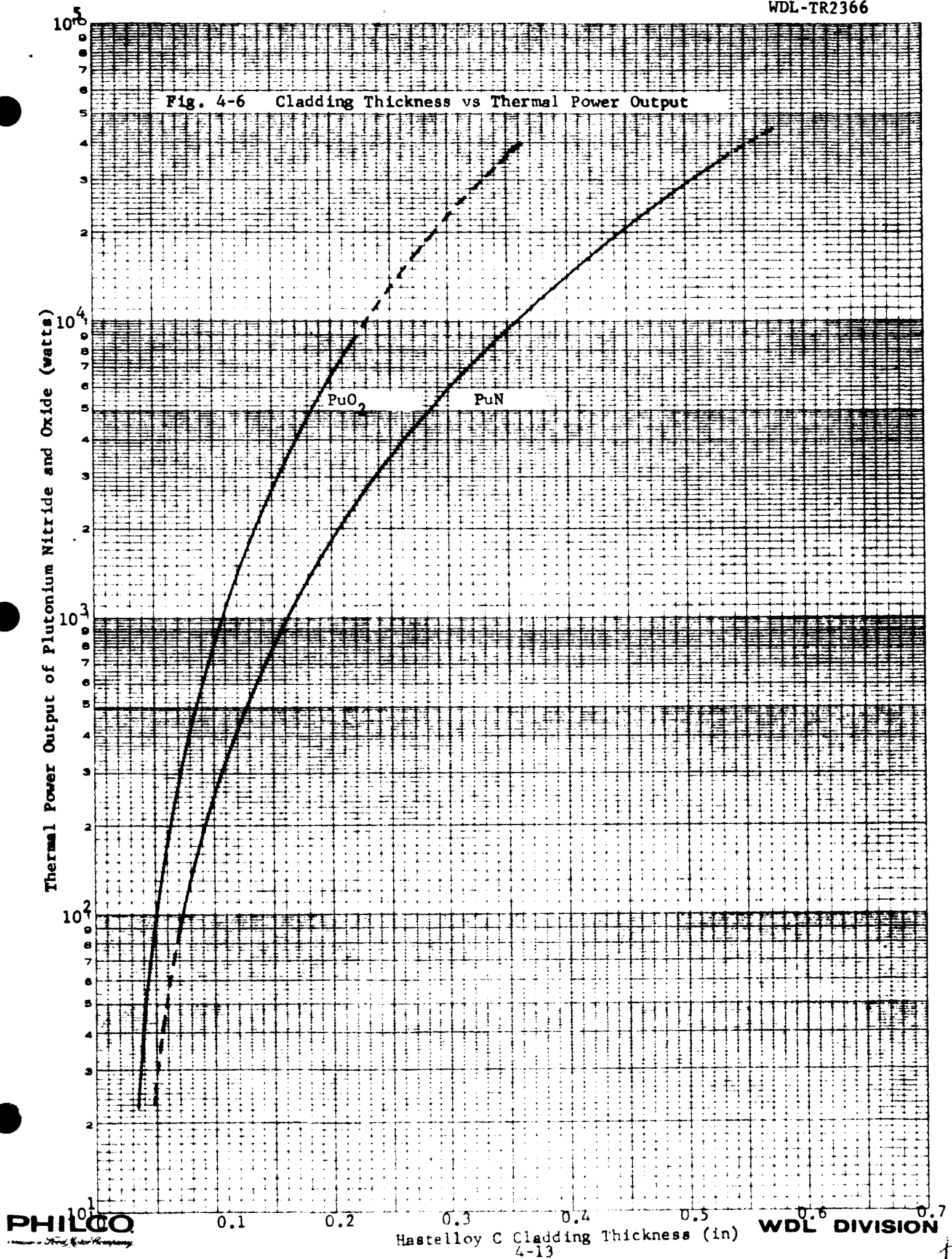


Performance Parameters

Parametric calculations are displayed in a series of figures intended to allow flexibility for changing power requirements and technology over the next ten years. The variable "thermal power output" is used instead of "electrical power available" to allow changes in conversion efficiencies to be incorporated with a minimum of inconvenience. Figure 4-5 shows the weight of isotopic compound, cladding, and total heat source for plutonium oxide. The required thickness of cladding to survive impact at terminal velocity is plotted in Figure 4-6 for both plutonium oxide and plutonium nitride. The nitride form may contain its own helium, thus obviating the requirement for a void volume in the fuel capsule. Figure 4-7 shows the weight of plutonium nitride, cladding, and total heat source for that compound. As cold-junction temperatures are lowered, the radiating area must be increased. Figure 4-8 shows fin weight vs. cold-junction temperature for four levels of thermal power output.

For a 600°F cold-junction fin system, Figure 4-9 presents the range of weights of heat source, insulation, casing, thermoelectric units, fins, power conditioner, and miscellaneous springs, shoes, solder, and straps. Total RTG weight as a function of thermal power is shown in the upper curve.

A compound of plutonium is ideal from the standpoint of radiation hazards and will require no additional shielding to protect personnel. Extremely sensitive instruments may, however, require shielding to reduce radiation-induced noise. Plutonium will be an expensive isotope to use in RTG units until wider use of nuclear reactor energy sources comes into being throughout the world. A comparison of 1968 costs, weight, and lead shielding required to provide similar gamma doses has been made for



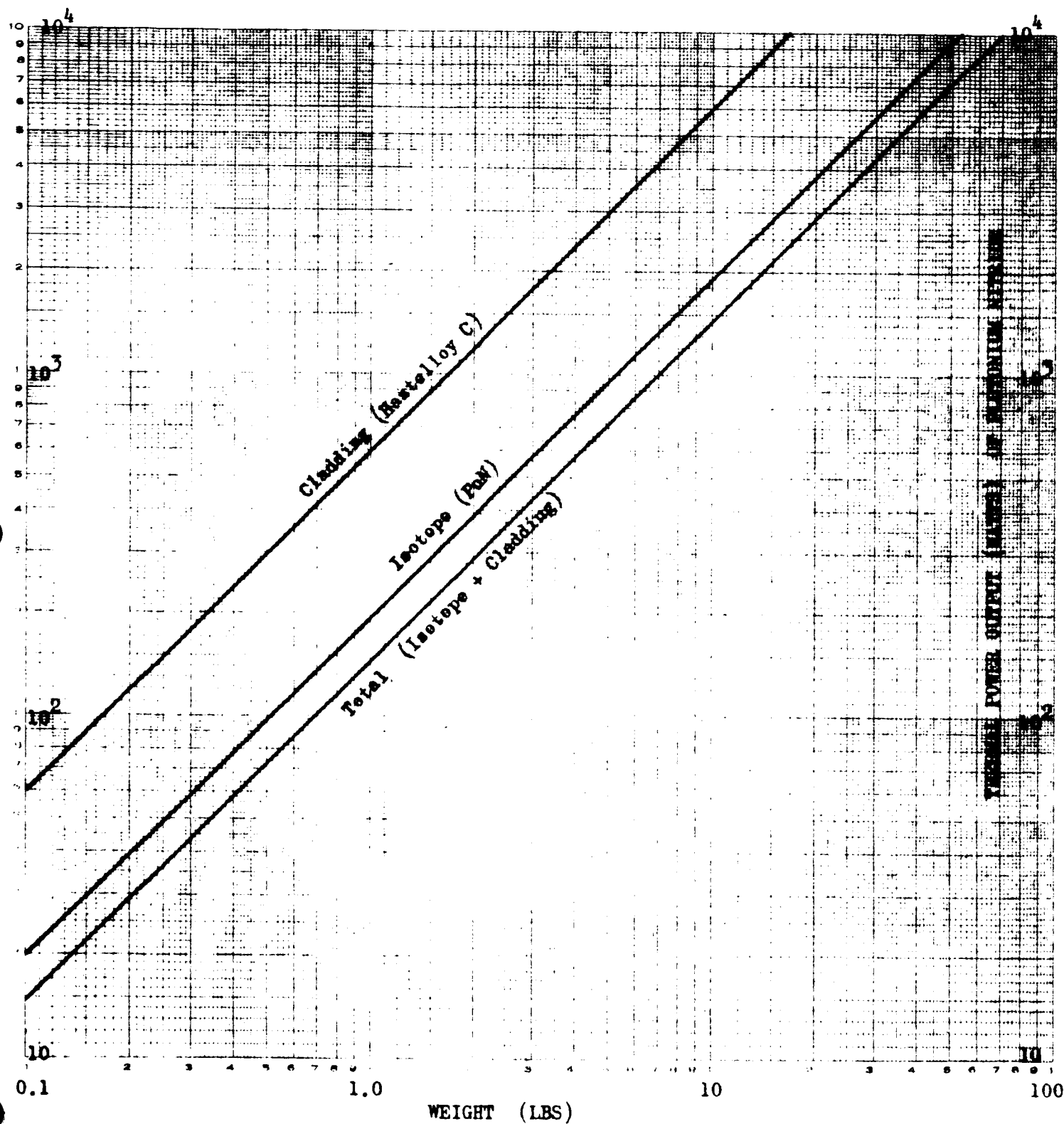
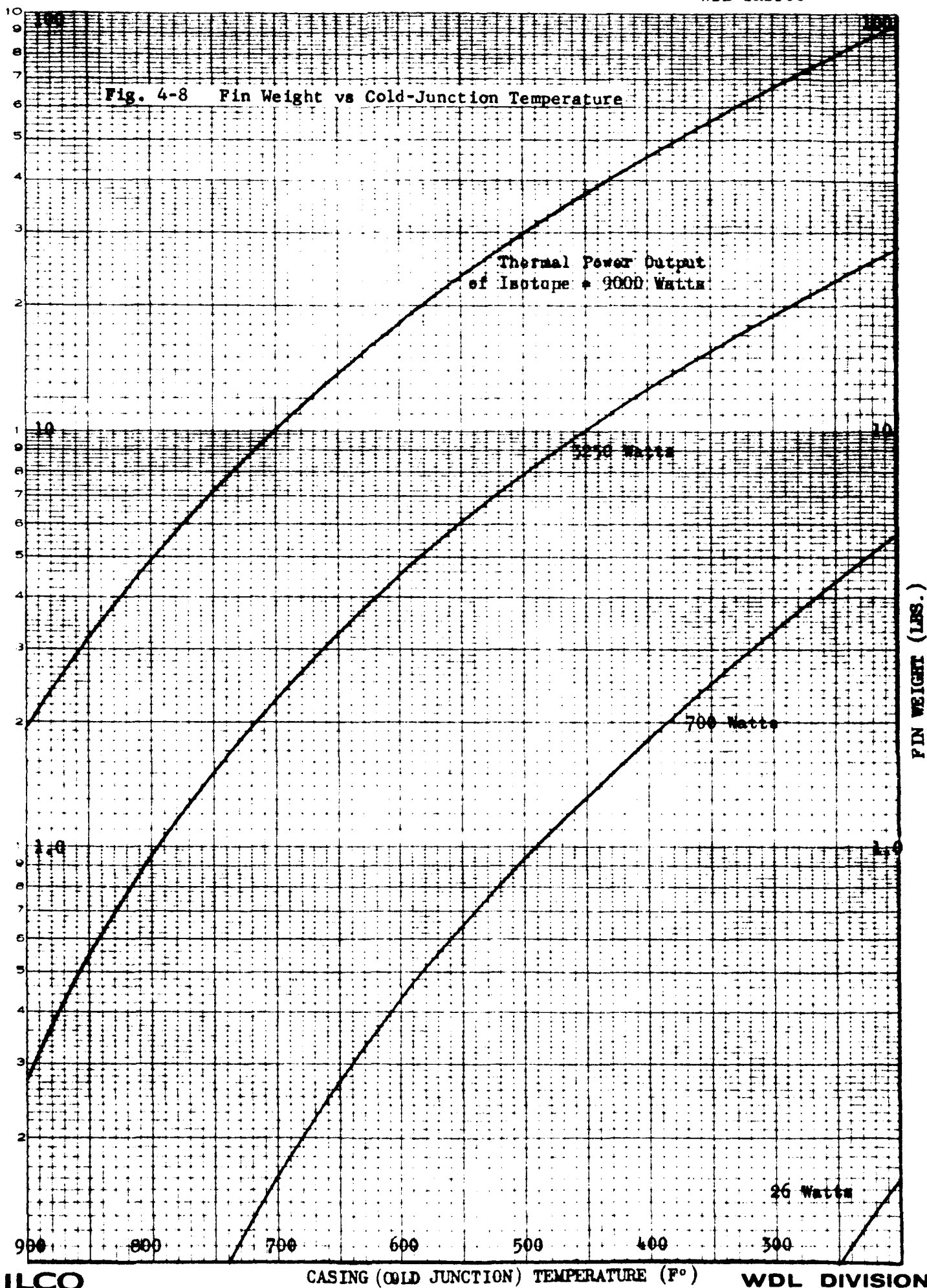


Fig. 4-7 Weight of Isotope, Cladding, and Total Heat Source vs. Thermal Power Output for Plutonium Nitride



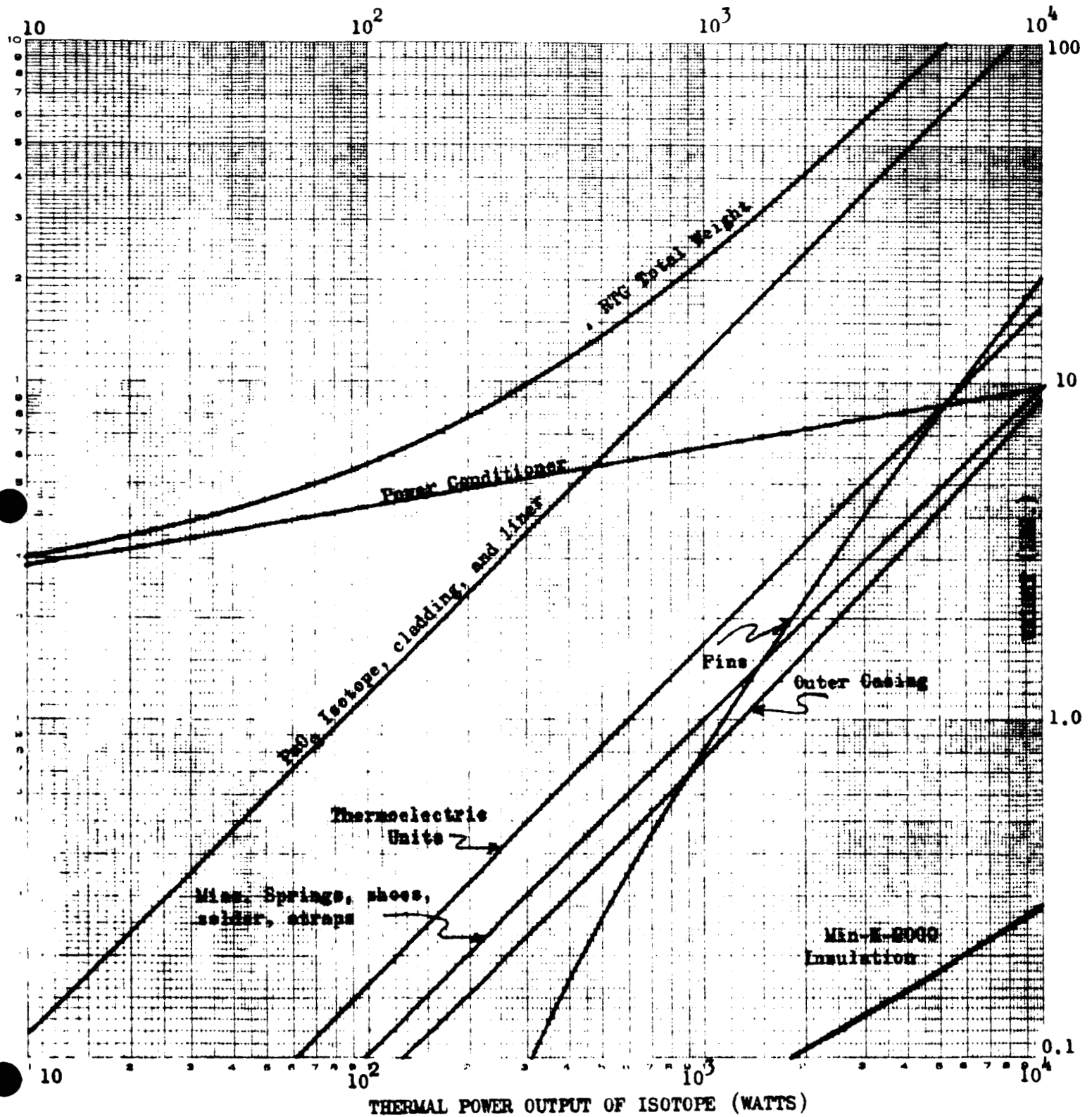


Fig. 4-9 Component Weight of RTG as a Function of Power

WDL by Battelle and is tabulated below:

ISOTOPE	WEIGHT (lb)	SHIELDING (cm of lead)	COST (1968)
Pu-238 PuN	20	0	\$3,600,000
Pm-147 Pm ₂ O ₃	40	4.6	\$ 465,000
Cm-244 Cm ₂ O ₃	3.8	9.5	\$1,570,000

SECTION 5

OPTIMUM SHIELDING CONFIGURATIONS

5.1 INTRODUCTION

The problem of shielding is present in nearly all situations involving radiation. Electrons, protons, and alpha particles are the most ionizing and damaging to man, but are the easiest shielded of particles of concern to spacecraft research and development. Neutrons and gamma rays are the most difficult to shield. This study has been concerned with the shielding of gamma radiation from radioisotopic power subsystems in spacecraft where excess weight is still an undesirable luxury.

The interaction of gamma photons with matter occurs by three processes: the photoelectric effect, the Compton effect, and pair production. The probability that one of these effects will remove a photon from its path through the material depends on the energy of the photon and the density of matter along its route. "Scattering" is said to occur when Compton interaction takes place and a new photon appears at an angle to the original ray path. For extended (i.e., not "point") sources and detectors (i.e., sensitive instruments), photons which would not have reached the detector in a narrow-beam geometry are scattered back and are registered. Thus there is an apparent build-up of dose above that calculated by the simple exponential attenuation law. This increased dose has been included in calculations by various forms of a multiplier called a "build-up factor", which depends on photon energy and shield thickness.

The current technique for creating a minimum-weight shield is the concept of "shadow" shielding. This approach has a degree of application for non-isotropic radiation fields such as those generated by radioactive isotopes, nuclear reactors, and X-ray generators. For a non-vacuum

environment, like an earth laboratory, air-scattering effects limit the usefulness of a shadow shield. On a spacecraft, even with air-scattering effects eliminated, parts of the vehicle become radiation scatterers. This problem can be alleviated by careful design. Finally, there is the shield itself to be considered as a scattering medium as well as an absorbing medium.

5.2 RESULTS OF STUDY

5.2.1 Two-Dimensional Problem

Figure 5-1 shows a line isotope with a finite number of radioactive atoms lined up evenly and emitting gamma rays. From the diagram, a varying "density" of rays can be observed between the isotope and line detector. The density is greatest in the center and diminishes uniformly toward both ends. A shield located at the center of the separating region might, from physical considerations, be expected to appear lens-shaped as shown. The taper from center to edge, neglecting build-up factor (i.e., multiple gamma scattering), can also, from physical considerations, be shown to be logarithmic.

The simple ray picture can be applied to show how the shield-shape changes with location, as indicated in Figure 5-2. For the symmetrical situation, where source and detector are of equal size, the minimum weight shield is exactly centered. The maximum thickness portion increases as one moves away from the center in either direction. For certain prescribed doses, no shield is required. As doses are set smaller and smaller, a shield becomes necessary and the optimum weight shield starts as a mass in the center and grows outward. Figure 5-3 shows shields with attenuations of $1/3$, $1/10$, and $1/100$ without build-up factor.

The presence of a build-up factor to include the effects of gamma scattering for extended sources and detectors is important. The comparison for aluminum shielding (for which build-up factor data is readily available) with and without build-up factor is shown in Figure 5-4. It is

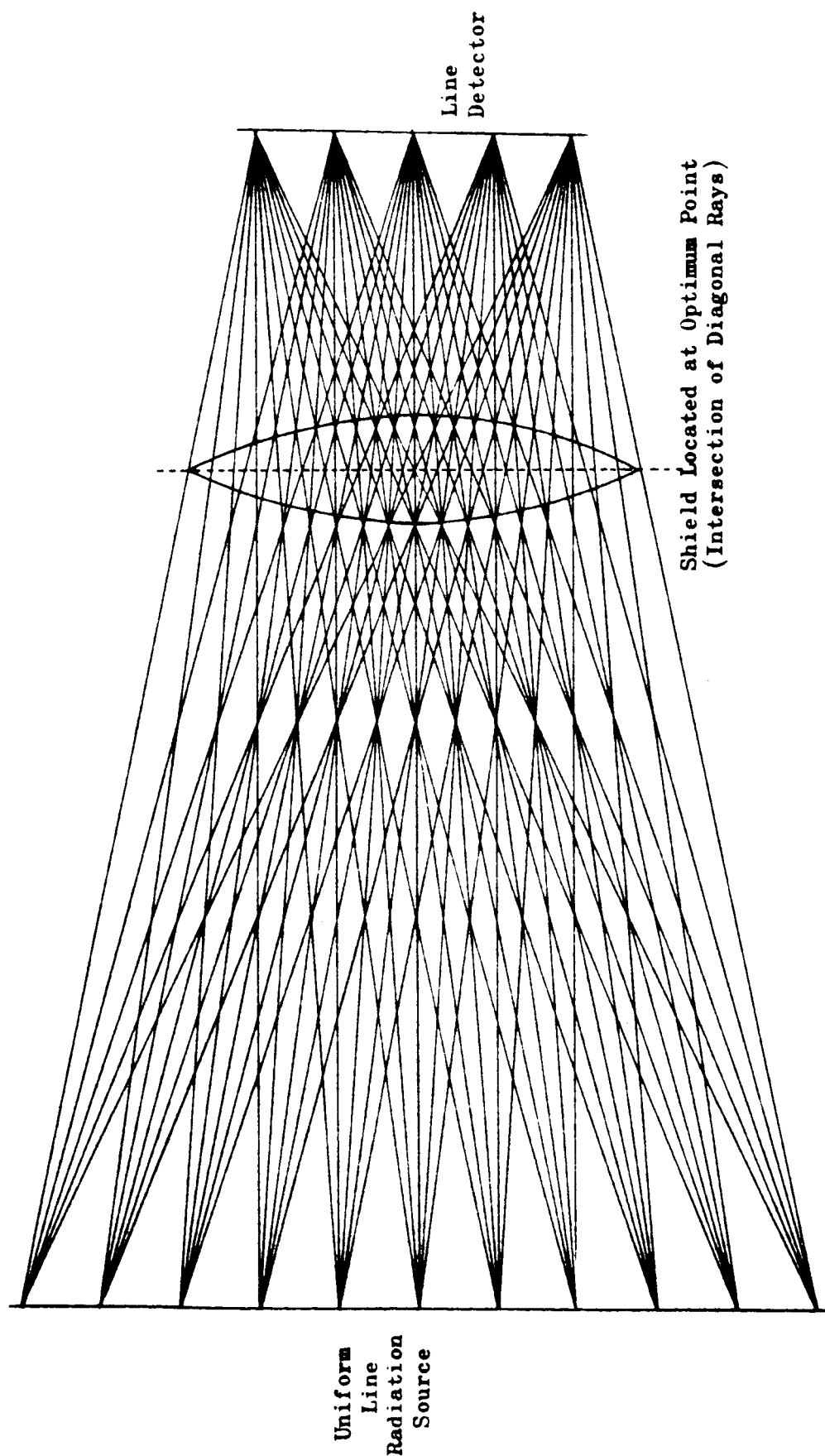


Fig. 5-1 RAY DENSITY BETWEEN SOURCE AND DETECTOR

The density of radiation is greatest along the horizontal center and diminishes towards top and bottom. At the intersection of the diagonal rays the density change is uniform and linear.

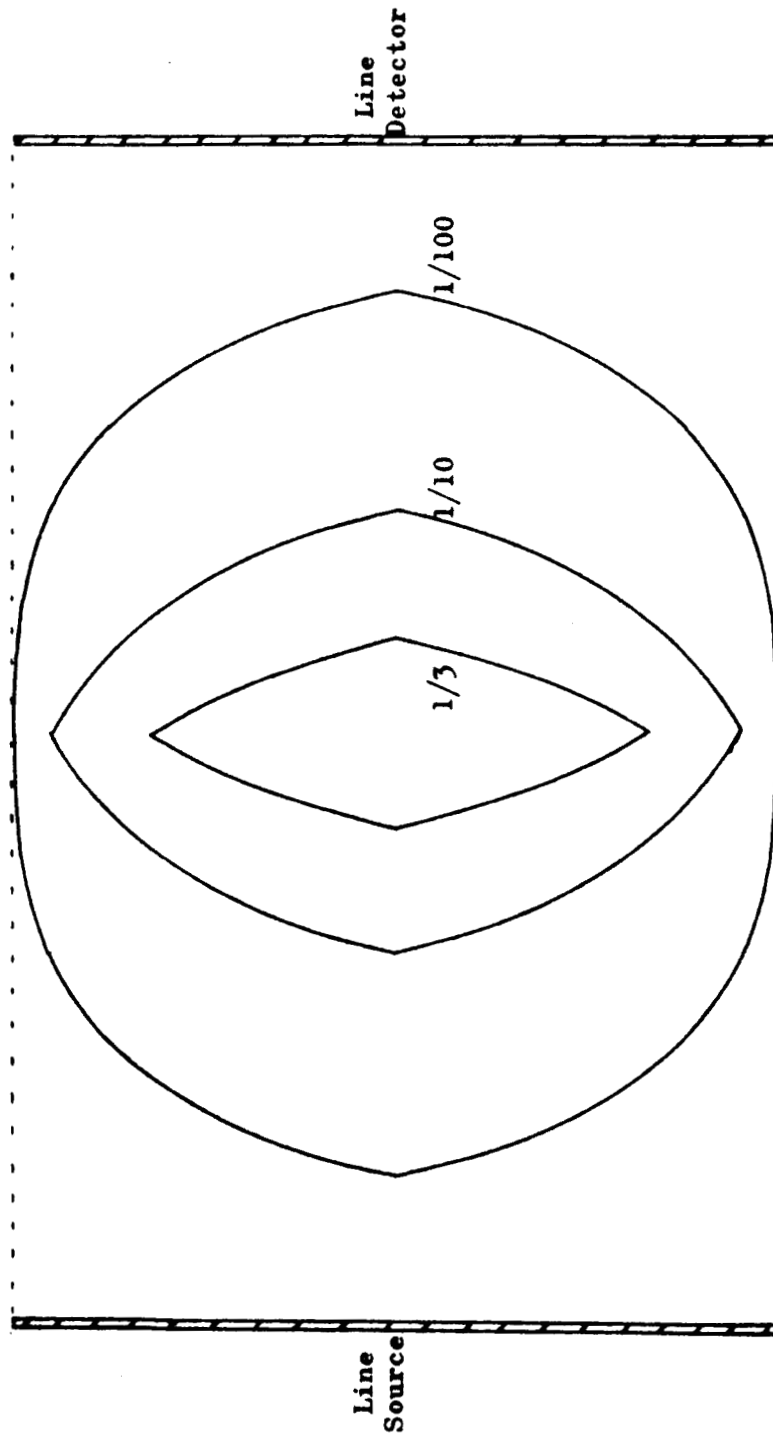


Fig. 5-3 CHANGE OF WEIGHT OPTIMIZED SHIELD WITH ATTENUATION FACTOR

Relative shapes of shields with B-1 at the intersection of the diagonal rays for three attenuation factors. For a small attenuation, the minimum weight shield does not extend to the geometrical limit (dotted line) of the radiation.

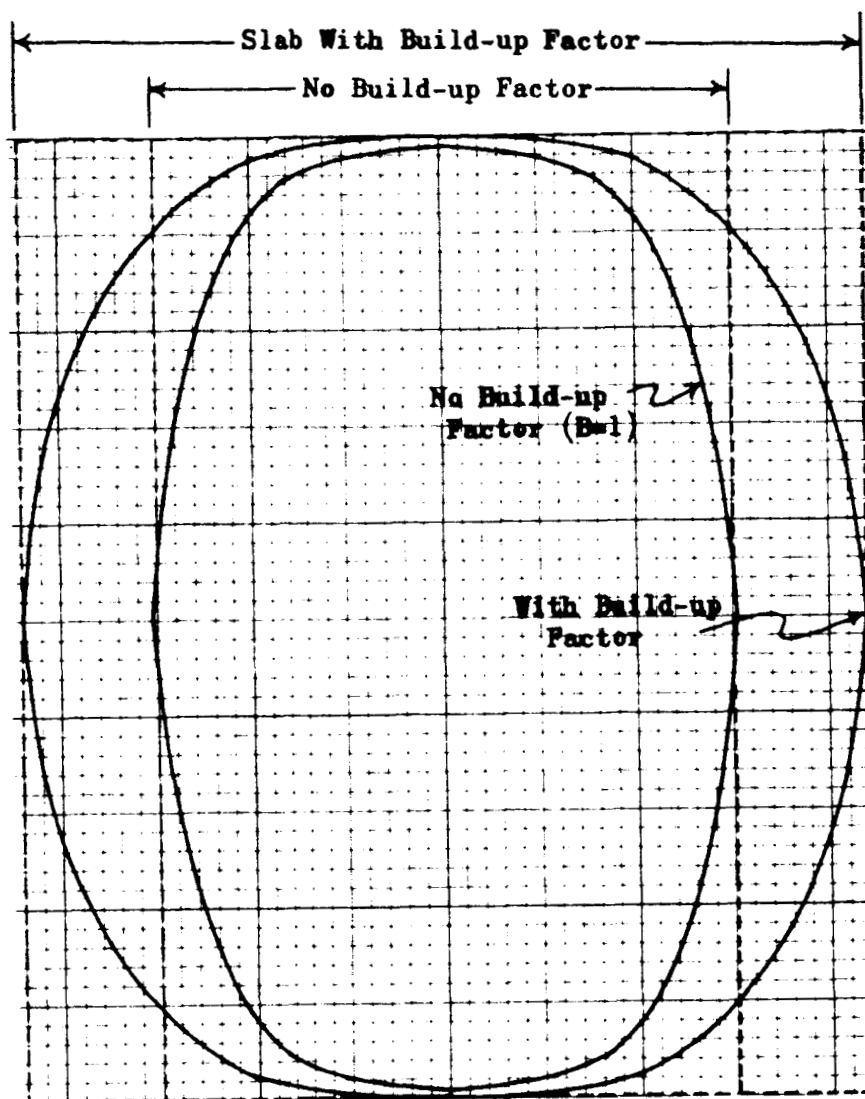


Fig. 5-4 COMPARISON OF OPTIMUM SHIELDS
CALCULATED WITH AND WITHOUT BUILD-UP FACTORS

Both figures are located at the intersection of the diagonal rays. The outer shield uses the build-up factor for aluminum with 1.25 Mev gamma rays. Conventional slab shielding for both cases is indicated by the dotted line.

observed that shape perturbing factors in the equation with build-up factor are not significant; the lens-like character remains unchanged. The thickness at the center increases as does the constant thickness of the simple slab.

A comparative weight calculation is easily accomplished for the two-dimensional plane shield by integration:

$$\frac{W(\text{plane slab})}{W(\text{optimized shield})} = \frac{\rho t x}{\rho \int t(x) dx} = \frac{t x}{\int \frac{1}{\mu \rho} \ln \Gamma(f + gx) dx} = 1.23 \quad (5-1)$$

A three-dimensional estimate might be made by rotating the two-dimensional solution about its axis of symmetry. This would be expected to produce a larger weight ratio since maximum thickness occurs in the center region.

$$\begin{aligned} \frac{W(\text{cylindrical slab})}{W(\text{rotated optimized shield})} &= \frac{\rho \pi x^2 t}{2\pi \rho \int t(x) x dx} \\ &= \frac{x^2 t}{2 \int \frac{x}{\mu \rho} \ln \Gamma(f + gx) dx} = 1.41 \quad (5-2) \end{aligned}$$

It is pointed out that these calculations are made with the optimized solution without build-up factor because it is considerably less formidable to integrate than the general solution. From Figure 5-4, it can be seen that this approximation is probably not far off since the general shape is very similar in both cases.

5.2.2 Three-Dimensional Problem

Time restrictions do not permit a complete exposition of a three-dimensional case in this report but it is felt that such a case, with

axial symmetry, would not be mathematically unwieldy. A conservative estimation of the weight comparison between simple slab shields and their optimized counterparts has been made in the previous section by rotating a "line" solution about a central axis. This weight comparison is thought conservative because the central portions of a circular shield will effect an even higher degree of shielding utility than a line shield in a comparable two-dimensional situation. A mental extrapolation of Figure 5-1 to a geometry of axial rotation may provide a more convincing argument by showing an even higher density of ray paths through the center as compared with regions in the vicinity of shield edges.

The two-dimensional example uses a "line" isotope as source and a line detector at which the maximum tolerable dose is initially prescribed. It will simplify the example considerably if the shield is also taken to be a line shield with variable density to be determined. If the resulting solution is then applied to a shield of uniform density material and the physical outline of the shield is allowed to vary (this is in the true spirit of this method), then the configuration will prove to be slightly conservative. This is because ray path lengths in the shield will be traversing a hypotenuse and will thus be greater than the direct path assumed in the formulation.

5.3 ANALYTICAL DEVELOPMENT

5.3.1 Outline of Technique

Given a prescribed radiation dose at the detector, one desires to find a minimum weight shield to be placed between the radiation source and the detector with the required attenuation characteristics. The general approach to solving this problem is as follows:

1. Express the shield weight as an integral of a function of thickness over the shield area ($dA = du dv$, where u and v are transverse coordinates):

$$W = \int w(t) dA. \quad (5-3)$$

2. Express the dose at the detector as a double integral over the source and detector surfaces, where the integrand is again a function of shield thickness.

$$\begin{aligned} D &= \int_s \int_d S B(t) r^{-2} e^{-\alpha t} dA_s dA_d \\ &= \int_s \int_d d(t) dA_s dA_d \end{aligned} \quad (5-4)$$

where S , B , α , and r are conventional notations, respectively, for source strength per unit area, build-up factor, gamma attenuation coefficient, and ray path length.

3. Transform the dose integral to a single integral over the shield area

$$D = \int f(A, t(A)) dA. \quad (5-5)$$

4. Combine the two functions using the method of Lagrange multipliers appropriate to a variational approach,

$$I = W + \lambda D$$

$$= \int [w(t) + \lambda f(A, t(A))] dA \quad (5-6)$$

5. Applying the techniques of the calculus of variations, set the first variation of I equal to zero and solve for $t(A, \lambda)$. Since the integrand has no dependence on the derivatives of t , the Euler-Lagrange equations, resulting from the variation of I , are particularly simple.

$$\delta I = 0 \quad \text{produces}$$

$$\frac{\partial}{\partial t} [w(t) + \lambda f(A, t)] = 0 \quad (5-7)$$

6. The solution for thickness as a function of area coordinates and the Lagrange constant is obtained algebraically.

$$t = t(A, \lambda) \quad \text{where } t \geq 0. \quad (5-8)$$

Physically, the thickness cannot be negative, whence the latter restriction on t . The constant λ may be evaluated by intuition in certain configurations, or by formally carrying out the dose integral with the proper limits

of integration

$$D = \int f(A, t(A, \lambda)) dA \quad (5-9)$$

where D is a given constant for the problem.

The integral may be in two main parts; the first extending from $A = 0$ to an upper limit where t becomes zero, and the second extending from this point to the upper geometrical limit.

The relation $t = t(A, D)$ is the complete and optimal solution to the shielding problem. It is the equation for the shape (i.e. the outline) of the minimum weight shield which removes all radiation above a given permitted dose (or dose rate).

5.3.2 Transformation to Shield Coordinates

The weight integral is expressed simply as follows:

$$W = \int \rho(x) t \, dx \quad (5-10)$$

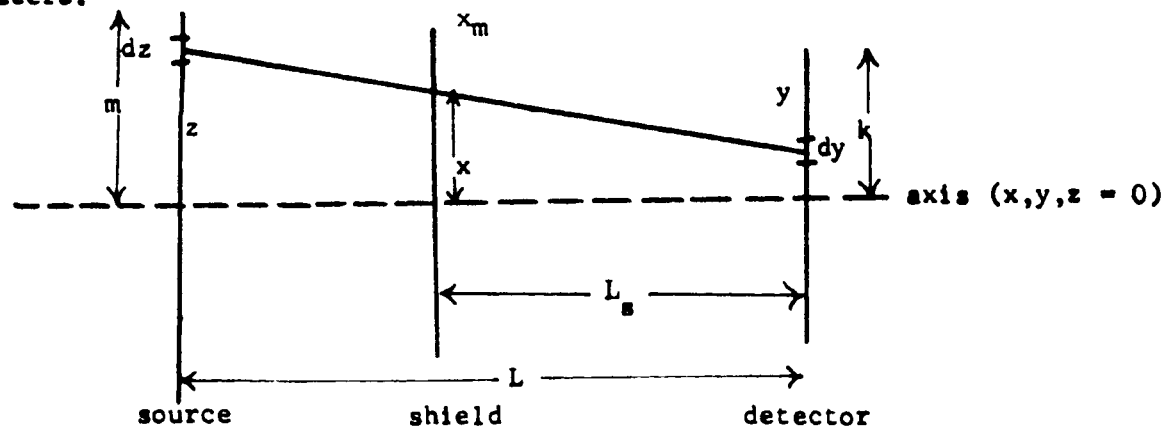
or, retaining ρ as a constant and letting t be the variable (these quantities always appear together as the product ρt),

$$W = \int \rho t(x) \, dx \quad (5-11)$$

The latter expression is the preferable one.

$$D = S \int_{-k}^k \int_{-m}^m dz B(t) r^{-2} e^{-\mu \rho t} dy \quad (5-12)$$

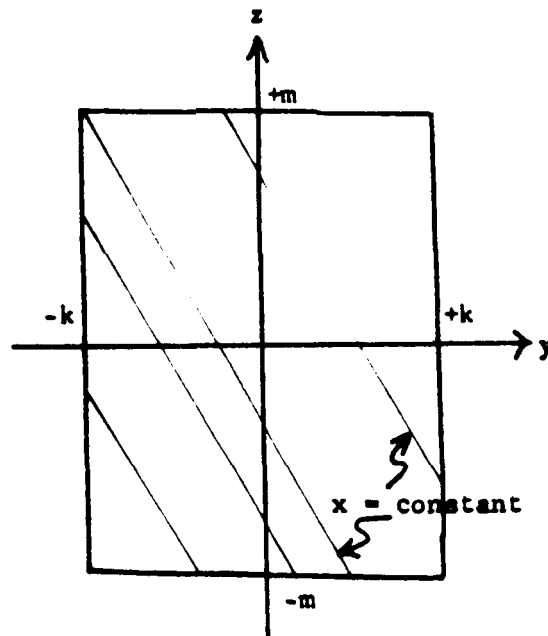
where t is the shield thickness, x the location on the shield with respect to the center, D the dose or dose-rate initially set at the detector, S the source strength of the isotope in photons per unit area per steradian, z the location on the source referenced to the center, B the build-up factor to incorporate the effects of multiple scattering, r the ray path length, μ the mass attenuation coefficient for the shield in area per mass units, ρ the density, and y the location on the detector referenced to the center. The sketch below also illustrates the parameters.



To transform the dose integrals over y and z to an equivalent integral over x , we obtain from the diagram above,

$$\begin{aligned}
 x &= y + \frac{z - y}{L} L_s \\
 &= \frac{L_s}{L} z + \left(1 - \frac{L_s}{L}\right) y \\
 &= a z + b y
 \end{aligned}
 \tag{5-13}$$

where a and b are defined by the relations above. Lines of constant x can be drawn on a y - z plane with slope $\frac{dz}{dy} = -\frac{b}{a}$.



Lines perpendicular to $az + by = x$ are the set $bz - ay = w$ with slope $\frac{dz}{dy} = \frac{a}{b}$.

We are effectively going to rotate the coordinates from a y - z orientation to an x - w orientation. We can then integrate over w , since x will be constant over this integration, and leave an integration over x to be performed. This is the formulation in which we desire the dose integral to be stated.

From the transformation

$$x = a z + b y \quad (5-14)$$

$$w = b z - a y \quad (5-15)$$

we calculate the inverse transformation

$$y = \frac{a}{a^2 + b^2} x + \frac{b}{a^2 + b^2} w \quad (5-16)$$

$$z = \frac{b}{a^2 + b^2} x - \frac{a}{a^2 + b^2} w \quad (5-17)$$

and the Jacobian,

$$\begin{aligned} J &= \frac{\partial(y, z)}{\partial(x, w)} \\ &= \frac{-1}{a^2 + b^2} \end{aligned} \quad (5-18)$$

The dose integral changes as follows:

$$D = \int_{-m}^m \int_{-k}^k d(t(x), y, z) dy dz \quad (5-19)$$

$$= \int_{x_-}^{x_+} \int_{w_-}^{w_+} J d(t(x), w, x) dw dx \quad (5-20)$$

$$= \int_{x_-}^{x_+} f(t(x), x) dx \quad (5-21)$$

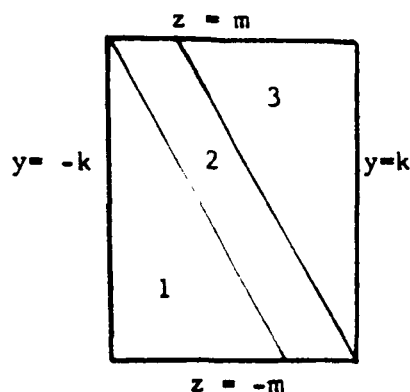
which is the desired form.

The limits of the integration over w form three groups,

depending at which boundaries the lines of constant x terminate.

It is observed that if the shield is placed exactly in the center

between the source and detector, then only two groups will result, separated by the diagonal.



For each group we apply the transformation equations (5-14) to (5-17) and tabulate the limits w_+ and w_- of the integral. For example, in group 1 the integration over w would terminate at each end of a line of constant x ; from the line $y = -k$ to the line $z = -m$. At $y = -k$ we find that $z = \frac{x}{b} + \frac{ak}{b}$, and at $z = -m$ we find that $y = \frac{x}{a} + \frac{bm}{a}$; thus $w_+ = -bk - \frac{a}{b}(x + ak)$ and $w_- = am + \frac{b}{a}(x + bm)$.

GROUP	UPPER LIMIT	LOWER LIMIT
1	$w_+ = -bk - \frac{a}{b}(x + ak)$	$w_- = am + \frac{b}{a}(x + bm)$
2	$w_+ = -am + \frac{b}{a}(x - bm)$	$w_- = am + \frac{b}{a}(x + bm)$
3	$w_+ = -am + \frac{b}{a}(x - bm)$	$w_- = bk - \frac{a}{b}(x - ak)$

The general solution will follow after a slight digression to explore two approximations which are useful.

Approximation if L is Large

A simplification enters if the integrand $d(t(x), y, z)$ is not a function of y and z . This would occur if there was no r^2 dependence. This is almost the case if L is large compared with m and k , whence $r^2 = L^2$. In space vehicles m is on the order of 5 cm, and L is on the order of 1 meter, so the approximation is nearly justified.

$$D = \int \int L^{-2} S B(t) e^{-\mu \rho t} dy dz \quad (5-22)$$

$$= \int J L^{-2} S B(t) e^{-\mu \rho t} \int_{w_-}^{w_+} dw dx$$

$$= \int J L^{-2} S B(t) e^{-\mu \rho t} (w_+ - w_-) dx \quad (5-23)$$

In general, the difference of the limits is a linear function of x ,

$$w_+ - w_- = f + g x \quad (5-24)$$

where f and g depend on group location and are tabulated below for convenience.

GROUP	f	g
1	$-am - bk - \frac{b^2 m}{a} - \frac{a^2 k}{b}$	$-\frac{b}{a} - \frac{a}{b}$
2	$-2 am - 2 \frac{b^2 m}{a}$	0
3	$-bk - am - \frac{b^2 m}{a} - \frac{a^2 k}{b}$	$+\frac{b}{a} + \frac{a}{b}$

The integral to be operated upon in this approximation is

$$I = W + \lambda D$$

$$= \int \left[\rho^t(x) + \lambda L^{-2} S J B(t) e^{-\mu \rho^t} (f + gx) \right] dx \quad (5-25)$$

For $\delta I = 0$ we know that

$$\frac{\partial}{\partial t} \left[\rho^t(x) + \lambda L^{-2} S J B(t) e^{-\mu \rho^t} (f + gx) \right] = 0 \quad (5-26)$$

or

$$\rho + \lambda L^{-2} S J (f + gx) \left[\frac{\partial B}{\partial t} - \mu \rho B \right] e^{-\mu \rho^t} = 0 \quad (5-27)$$

In the case of $B = 1$ (no build-up factor, i.e. multiple scattering is neglected), the equation simplifies again.

$$\rho - \lambda L^{-2} S J (f + gx) \mu \rho e^{-\mu \rho^t} = 0 \quad (5-28)$$

$$e^{-\mu \rho^t} = \frac{\rho}{\lambda L^{-2} S J \mu \rho (f + gx)} = \frac{1}{\Gamma (f + gx)}$$

$$-\mu \rho^t = -\ln (f + gx) \Gamma$$

$$t = \frac{1}{\mu \rho} \ln \Gamma (f + gx)$$

(5-29)

This solution is plotted in Figure 5-3 for $L_s/L = a = \frac{1}{2}$ and for attenuations of $1/3$, $1/10$, and $1/100$.

In the case that $B \neq 1$, and $r^2 = L^2$, we can still develop an interesting relation between t and x . Let us first examine various forms of B to find a form which gives adequate accuracy and

ease of handling. These are listed in Table 5-1.

Table 5-1 Forms of Build-up Factor [Hubbell; 1963]

- ### 1. Linear (one parameter)

$$B = 1 + p \mu \rho t$$

- ## 2. Exponential-Linear (two parameters)

$$B = 1 + p \mu \rho t e^{-q \mu \rho t}$$

- ### 3. Exponential-Polynomial (1 to 3 parameters)

$$B = (pt^2 + qt + r) e^{+\mu\varphi t}$$

- #### 4. Low order Polynomial (3 parameters)

$$B = 1 + p\mu\tau + q(\mu\tau)^2 + r(\mu\tau)^3$$

- ### 5. Sum of Exponentials (3 parameters)

$$B = p e^{-q\mu\tau} + (1-p) e^{-r\mu\tau}$$

- ## 6. Exponential-Linear Moments (4 parameters)

$$B = 1 + \mu_{\rho t} \left[p_q e^{\mu_{\rho t}(1-q)} + r_s e^{\mu_{\rho t}(1-s)} \right]$$

The linear form is very useful for penetrations up to two mean free paths (i.e. $\mu_{pt} \leq 2$), but deviates from experiment by -13% at $\mu_{pt}=4$ for aluminum [Hubbell; 1963]. Using this in Equation (5-27), we obtain

$$\rho + \lambda L^{-2} S J (f + gx) [p\mu\rho - \mu\rho(1 + p\mu\rho t)] e^{-\mu\rho t} = 0 \quad (5-30)$$

or

$$f + gx = \frac{-\rho L^2 e^{\mu \rho t}}{J \lambda S \mu \rho [p - (1 + p \mu \rho t)]} \quad (5-31)$$

which is of the form

$$x = \alpha + (\beta - \gamma t)^{-1} e^{\delta t}. \quad (5-32)$$

This equation may be solved explicitly for $x(t)$ and used from a graph to obtain $t(x)$.

The two-parameter exponential-linear form of the build-up factor is surprisingly good for penetrations up to ten mean-free-paths. For $\mu \rho t = 10$ in aluminum the deviation from experiment is everywhere less than $\pm 6.4\%$. From the build-up factor expression,

$$B = 1 + p \mu \rho t e^{-q \mu \rho t},$$

$$\frac{\partial B}{\partial t} = (1 - \mu \rho q) p \mu \rho e^{-q \mu \rho t} \quad (5-33)$$

Using this in Equation (5-27),

$$\rho + \lambda L^{-2} S J (f + gx) \left[(1 - \mu \rho q) p - (e^{q \mu \rho t} + p \mu \rho t) \right] \mu \rho e^{-\mu \rho t(1+q)} = 0$$

or

$$f + gx = \frac{-\rho L^2}{\lambda S J \mu \rho [p(1 - \mu \rho q) - p \mu \rho t] e^{-\mu \rho t(1+q)} - \lambda S J \mu \rho e^{-\mu \rho t}} \quad (5-34)$$

which is of the form

$$x = \alpha + \frac{1}{(\epsilon + \eta t) e^{\theta t} - \sigma e^{\phi t}}. \quad (5-35)$$

5.3.3 Exact Solution

The general solution, of course, includes a $1/r^2$ dependence which becomes important as m/L or k/L approaches one.

$$D = S \int \int dz B(t) r^{-2} e^{-\mu \eta t} dy \quad (5-12)$$

The integrand must again be expressed in terms of w and x so that the w integration can be carried out.

$$r^2 = (y - z)^2 + L^2 \quad (5-36)$$

$$\begin{aligned} &= \left(\frac{a-b}{a^2+b^2} x + \frac{a+b}{a^2+b^2} w \right)^2 + L^2 \\ &= A + B w + C w^2 \end{aligned} \quad (5-37)$$

where

$$A = \left(\frac{a-b}{a^2+b^2} \right)^2 x^2 + L^2 \quad (5-38)$$

$$B = \frac{2(a^2 - b^2)}{(a^2 + b^2)^2} x \quad (5-39)$$

$$C = \frac{1}{(a^2 + b^2)^2} = J^2 \quad (a + b = 1) \quad (5-40)$$

and if the algebra is being followed, it should be observed that $a - b = a^2 - b^2 = 2a - 1$, and J comes from Equation (5-18) for the Jacobian of the transformation.

The integral of interest is

$$K(x) = \int_{w_-}^{w_+} \frac{dw}{A + B w + C w^2} \quad (5-41)$$

$$K(x) = 2 (4AC - B^2)^{-\frac{1}{2}} \arctan (2Cw + B)(4AC - B^2)^{-\frac{1}{2}} \Big|_{w_-}^{w_+} \quad (5-42)$$

where

$$(4AC - B^2)^{\frac{1}{2}} = \frac{2L}{a^2 + b^2} = -2JL \quad (5-43)$$

Thus,

$$K(x) = \frac{-1}{JL} \left[\arctan \frac{2J^2 w_+ + 2J^2 (a^2 - b^2) x}{-2JL} - \arctan \frac{2J^2 w_- + 2J^2 (a^2 - b^2) x}{-2JL} \right] \quad (5-44)$$

Since all the w limits are linear in x , we can write

$$K(x) = - (JL)^{-1} \left[\arctan (D + Ex) - \arctan (F + Gx) \right] \quad (5-45)$$

where D, E, F, G once again depend upon group location as defined in the previous section and are tabulated below.

GROUP	F	G	D	E
1	$\frac{-m}{La}$	$\frac{J}{L}(a-b+\frac{b}{a})$	$\frac{+k}{Lb}$	$\frac{J}{L}(a-b-\frac{a}{b})$
2	$\frac{-m}{La}$	$\frac{J}{L}(a-b+\frac{b}{a})$	$\frac{+m}{La}$	$\frac{J}{L}(a-b+\frac{b}{a})$
3	$\frac{-k}{Lb}$	$\frac{J}{L}(a-b-\frac{a}{b})$	$\frac{+m}{La}$	$\frac{J}{L}(a-b+\frac{b}{a})$

Again we take the first variation of the integral made up of the weight plus a constant times the dose function.

$$I = W + \lambda D$$

$$= \int \left[\rho^t(x) + \lambda K(x) \text{SJB}(t(x)) e^{-\mu \rho^t} \right] dx \quad (5-46)$$

For $\delta I = 0$,

$$\frac{\partial}{\partial t} \left[\rho^t + \lambda K \text{SJB} e^{-\mu \rho^t} \right] = 0 \quad (5-47)$$

or

$$\rho + \lambda K \text{SJB} \left[\frac{\partial B}{\partial t} - \mu \rho B \right] e^{-\mu \rho^t} = 0. \quad (5-48)$$

Using the exponential-linear approximation to the build-up factor, the bracket becomes

$$\left[\frac{\partial B}{\partial t} - \mu \rho B \right] = \left[p e^{-q \mu \rho^t} - q \mu \rho e^{-q \mu \rho^t} - 1 - p \mu \rho^t e^{-q \mu \rho^t} \right] \mu \rho \quad (5-49)$$

The general relation may be written as

$$K(x) = \frac{-\rho}{\lambda \text{SJB} \mu \rho \left[p(1 - \mu \rho^q) - \mu \rho^p t \right] e^{-\mu \rho^t(q+1)} - \lambda \text{SJB} \mu \rho e^{-\mu \rho^t}} \quad (5-50)$$

which is of the following form, and solvable by iteration techniques:

$$\arctan(\alpha + \beta x) - \arctan(\gamma + \delta x) = \frac{1}{(\epsilon + \eta t) e^{\theta t} - e^{\phi t}}$$

(5-51)

SECTION 6

CONCLUSIONS AND RECOMMENDATIONS

6.1 PHOTOVOLTAIC-ISOTOPIIC COMPARISON

The physical characteristics and performance capabilities of the photovoltaic and isotopic power configurations are tabulated and compared in Table 6-1.

6.1.1 Photovoltaic Power

The photovoltaic power subsystem possesses the following advantages:

1. Proven reliability
 - a. Almost all spacecraft requiring relatively small power levels over long periods have utilized photovoltaics with excellent results.
 - b. Almost all systems now in preparation plan to use photovoltaics, specifically silicon cells.
 - c. It is a relatively simple static system.
2. All components are readily available
 - a. No lengthy, costly developmental program necessary.
3. Potential improvements
 - a. Small increase in large quantity cell efficiencies can be anticipated.
 - b. Improved manufacturing methods should lead to cost reduction.
 - c. Integral cell covers could lead to substantial fabrication cost reductions.

Table 6-1 Comparison of Photovoltaic and Isotopic Power Subsystems
(200 watts)

PARAMETERS	PHOTOVOLTAIC*	ISOTOPIC
Specific Weight	1.68 - 1.24 watts (e)/lb	1.8 watts (e)/lb
Weight - Pons-Winnecke - Brooks (2)	119 lbs 162 lbs	110 lbs 110 lbs
Shroud - Pons-Winnecke - Brooks (2)	R&D envelope Surveyor envelope	R&D envelope R&D envelope
Reliability	Simple, static system Flight proven assemblies	Static system Not yet flight proven
Component Availability	Off-the-shelf components	Developmental stage
Dust Erosion	Small power degradation	No effect
Solar Flare Effects	Degrades power; can be ** minimized by cover glass	No degradation
Hazards	No special ground handling No abort precautions necessary No shielding of S/C components	RTG must be cooled on the pad Abort casing required Shielding of S/C may be necessary depending on isotope***
Mission Adaptability	Panel varies with mission	Size independent of sun distance
Growth Potential	Small increase in efficiency Moderate decrease in cost	Increase in specific weight to 5 w/lb projected for 1975

* Does not include batteries

** A 30-mil cover-glass thickness is assumed in the specific weight value

*** For Plutonium-238 minimum shielding is required

6.2 CHOICE OF POWER SUBSYSTEM

On the basis of a comparison between the performance of photovoltaic and isotopic power subsystems on a comet probe requiring 200 watts or more, photovoltaic panels are recommended for flights to comets out to heliocentric distances of about 1.6 A.U., e.g., Pons-Winnecke at 1.25 A.U. and Kopff at 1.57 A.U. On flights beyond 1.6 A.U., e.g., Brooks (2) at 1.8 A.U., photovoltaic panels are large but nevertheless desirable because of proven technology at a 200-watt power level. For higher powers (e.g., 300 watts), RTG units are recommended.

SECTION 7

REFERENCES

Anon., "MACS Solar Array Redesign Report," STL Report No. 8500.30-31; January 10, 1964.

Arvesen, J. C., Neel, C. B., and Shaw, C. C., "Preliminary Results from a Round-Robin Study of Ultraviolet Degradation of Spacecraft Thermal-Control Coating," Symposium on Thermal Radiation of Solids, San Francisco, California; March, 1964.

Baker, J. K., "Temperature Control Techniques for Solar Energy Converters," Technical Report ASD-TR-61-689; pp. 1-176; February, 1962.

Battelle Memorial Institute Radiation Effects Information Center, "Space-Radiation Damage to Electronic Components and Materials", Report No. 32; October 30, 1963.

Battelle, "Technical Proposal to NASA Manned Spacecraft Center for a Feasibility Study for a 50-watt(e) Integrated Power Unit to Operate on the Lunar Surface", August 20, 1964. (Philco WDL assisted in the preparation of this proposal and would be a subcontractor for this study).

Cherry, W., and Zontendyk, J. A., "The State-of-the-Art in Solar Cell Arrays for Space Electrical Power," AIAA Paper No. 64-738; September, 1964.

Cooley and Janda, Handbook of Space Radiation Effects on Solar Cell Power Systems, NASA SP-3003; (undated).

Garrett, W., and Turner, M. A., "Radiative Properties of Surface Finishes," General Electric Report PIR 9722-019, pp. 1-15; June, 1962.

Goedeka, A. D., "Radiation Shielding in Space Vehicles", Space Exploration Lecture No. 11, Engineering Extension and Physical Science Extension, University of California, Los Angeles, presented at NASA-Ames in Fall, 1962.

Hubbell, J. H., "A Power-Series Buildup Factor Formulation. Applications to Rectangular and Off-Axis Disk Source Problems," Journal of Research, National Bureau of Standards, vol. 67C, No. 4, p. 291; October-December, 1963.

Klein, D., and Nishina, Y., Z. Physik, vol. 52, p. 853; 1929.

Masley, A. J. and Goedeka, A. D., "Complete Dose Analysis of the November 12, 1960 Solar Cosmic-Ray Event," Douglas Aircraft Co., Report 1372; 1962. Also in Proceedings of the 3rd International Space Science Symposium, North-Holland Publ. Co., Amsterdam, 1963.

Menetrey, W. R., and Evans, W., "Energy Conversion Systems Reference Handbook", vol. V, WADD Technical Report No. 69-699; September, 1960.

Neel, C. B., "Research on the Stability of Thermal-Control Coatings for Spacecraft," NASA-Ames Report TMX-51, 196, pp. 1-26; October, 1963.

Philco, "Solar Probe Study Final Report," WDL TR-2133, Book B, Appendix 6, on NAS-2-1397; August 30, 1963.

Prince, M. B., "Silicon Solar Energy Converters," J. Appl. Phys., vol. 26, pp. 534-540; May, 1955.

Shirland, F. A., Wolff, G. A., Schaefer, J. C., and Dierssen, G. H., "Research on Solar-Energy Conversion Employing Cadmium Sulfide," ASD-TDR-62-69, vol. II, pp. 1-63, Harshaw Chemical Co., Cleveland, Ohio; December, 1962.

Singer, S. F., "High Energy Radiation Near the Earth", Astronautica Acta, Vol X./Fasc. 1; 1964.

Winkler, S. H., "Photovoltaic Space Power Systems," Course notes presented at University of Pennsylvania; June, 1962.

Wolf, M., "Limitations and Possibilities for Improvements of Photovoltaic Solar Energy Converters," Proc. IRE, vol. 58, pp. 1246-1263; July, 1960.

Zontendyk, J. A., Vondra, R. J., and Smith, A. H., "Mariner 2 Solar Panel Design and Flight Performance," Jet Propulsion Laboratory, Tech. Rept. 32-455, pp. 1-77; June 28, 1963.

APPENDIX A

CALCULATION OF SOLAR CELL DEGRADATION DUE TO PROTONS

A.1 DETERMINATION OF SUMMATION

The ratio of maximum power after irradiation to maximum initial power, P_m/P_{m0} , is related to the ratio of final to initial diffusion lengths in the solar cell. The radiation is producing traps (irregularities in the crystal structure) which cause an increasing number of electron-hole recombinations, thus reducing the maximum power output. The initial diffusion length, L_0 , is a property of the particular solar cell, and is usually in the range 150-275 microns. The effect of proton irradiation on diffusion length is determined from the following relation:

$$\frac{1}{L^2} = \frac{1}{L_0^2} + \sum_E k_p(E) \phi(E) \quad (A-1)$$

where L is the final diffusion length, $k_p(E)$ the energy-dependent damage coefficient, and $\phi(E)$ the total number of protons incident on a square centimeter with energy E .

The determination of the summation, $\sum k_p \phi$, can be a tedious job. A method is derived in this appendix to evaluate this quantity fairly rapidly and without introducing excessive error. The approach is to approximate the functions $k_p(E)$ and $\phi(E)$ as simple power functions of E which may be determined by measurements on their log-log graphs, and to accomplish a summation over infinitesimal energy intervals by integration. Where an entire spectrum cannot be well represented by a single straight line on a log-log plot, it can often be approximated to an adequate degree of accuracy by two or more such lines without becoming unwieldy.

The results of this derivation are as follows:

I. For $E < 28$ Mev:

$$\sum_{E_1}^{E_2} k_p \phi = \frac{5 \times 10^{-6} m}{m - 0.83} \left[\frac{N(>E_1) - N(>E_2)}{E_1^m - E_2^m} \right] \left[E_1^{m-0.83} - E_2^{m-0.83} \right] \quad (A-2)$$

II. For $E > 28$ Mev:

$$\sum_{E_1}^{E_2} k_p \phi = 1.5 \times 10^{-7} \left[N(>E_1) - N(>E_2) \right] \quad (A-3)$$

where m = "best" measured slope $\frac{\Delta N(>E)}{\Delta E}$ between E_1 and E_2 on a log-log plot of the integral spectrum of protons,
and $N(>E)$ = the number of particles with energy greater than E .

A.2 DERIVATION

1. Determination of Differential Spectrum from Integral Spectrum

Let $dN = n(E) dE$ = the number of particles with energy between E and $E + dE$.

The function $n(E)$ is called the differential spectrum and has the following properties:

$$N(E_1, E_2) = \int_{E_1}^{E_2} n(E) dE \quad \text{- number of particles with energy between } E_1 \text{ and } E_2$$

$$N(>E_1) = \int_{E_1}^{\infty} n(E) dE \quad \text{- number of particles with energy greater than } E_1$$

$$N(E_1, E_2) = N(>E_1) - N(>E_2).$$

If a portion of the integral spectrum, $N(>E)$ vs E , can be reasonably represented by a straight line on log-log graph paper, then within this region

$$N(>E) = A E^m$$

where m is the slope $\Delta N(>E)/\Delta E$ of the straight line representation.

The numerical value of m is easiest determined by measuring the linear distance (with a ruler) $\Delta N(>E)$ and dividing by the linear distance ΔE as measured with the same scale.

Since

$$N(>E_1) - N(>E_2) = A E_1^m - A E_2^m = \int_{E_1}^{E_2} n(E) dE$$

it is clear that by differentiation of $N(>E)$ we may determine $n(E)$.

$$n(E) = -m A E^{m-1}$$

The value of the constant, A , also follows

$$A = \frac{N(>E_1) - N(>E_2)}{E_1^m - E_2^m}$$

The quantity $n(E) dE$ will replace the entry ϕ in the summation.

2. Evaluation of an Equivalent Integral

The damage constant ⁽¹⁾ k_p can be represented by the following functions based on empirical data:

$$k_p = 5 \times 10^{-6} E^{-0.83} \quad \text{for } E < 28 \text{ Mev}$$

$$k_p = 1.5 \times 10^{-7} \quad \text{for } E > 28 \text{ Mev.}$$

The summation can now be replaced by an integral as follows:

$$\begin{aligned} \sum_{E_1}^{E_2} k_p \phi &= \int_{E_1}^{E_2} k_p n(E) dE \\ &= \int_{E_1}^{E_2} 5 \times 10^{-6} E^{-0.83} = A E^{m-1} dE \quad \text{for } E < 28 \text{ Mev} \\ &= 5 \times 10^{-6} = A \int_{E_1}^{E_2} E^{m-1.83} dE \\ &= \frac{5 \times 10^{-6} = A}{m - 0.83} E^{m-0.83} \Big|_{E_1}^{E_2} \end{aligned}$$

(1) Cooley and Janda, Handbook of Space-Radiation Effects on Solar Cell Power Systems, NASA SP-3003, 1963, Pg 25.

The author has used electron data to adjust Cooley and Janda's curve for 1 ohm-cm cells to apply to 10 ohm-cm cells, which are more radiation resistant.

$$= \frac{5 \times 10^{-6} m A}{m - 0.83} (E_2^{m-0.83} - E_1^{m-0.83})$$

Inserting the value of A, we obtain the desired result in terms of parameters of the integral spectrum.

$$\sum_{E_1}^{E_2} k_p \phi = \frac{5 \times 10^{-6} m A}{m - 0.83} \frac{N(>E_1) - N(>E_2)}{E_1^m - E_2^m} (E_1^{m-0.83} - E_2^{m-0.83})$$

for $E < 28$ Mev

The other energy range is more easily obtained:

$$\begin{aligned} \sum_{E_1}^{E_2} k_p \phi &= \int_{E_1}^{E_2} k_p n(E) dE \\ &= \int_{E_1}^{E_2} -1.5 \times 10^{-7} m A E^{m-1} dE \\ &= 1.5 \times 10^{-7} [N(>E_1) - N(>E_2)] \end{aligned}$$

for $E > 28$ Mev.

It should also be remembered that

$$\sum_{E_1}^{E_n} F(E) = \sum_{E_1}^{E_2} F(E) + \sum_{E_2}^{E_3} F(E) + \dots + \sum_{E_{n-1}}^{E_n} F(E).$$

APPENDIX B

MARTIN COMPANY RTG DESIGN

[This response to the WDL Comet Probe Solicitation by the Martin Company's Nuclear Division is classified Confidential according to AEC regulations, and is therefore contained in a separate classified supplement.]